6.4.2.1 Disposal System Geometry

A single disposal system geometry is used in the BRAGFLO computational model (see Appendix ***PA, Section PA-4.2*** ~~BRAGFLO~~) with four different maps of material properties: one for undisturbed conditions; one for the E1 intrusion event; ~~in which a borehole penetrates the panel and a Castile brine reservoir;~~ one for the E2 intrusion event~~, in which a borehole penetrates the repository but not a Castile brine reservoir~~; and one for the E1E2 intrusion event~~, in which at least one E1 borehole and one other borehole penetrate a disposal panel~~ (see Section 6.4.13.5). The geometry and material maps used in BRAGFLO are similar; each ~~is a~~ model***s*** ~~for~~ fluid flow calculations that represent~~s~~ the three-dimensional physical system in a two-dimensional plane ~~that cuts~~ ***cutting*** vertically through the repository and surrounding strata. Side views of the vertical cross section and two of the material maps are presented in Figures ~~6-13~~***6-14*** and ~~6-14~~***6-15***. In these figures, the boundaries of grid blocks discretized in the model ~~(see Appendix BRAGFLO, Section 4.5, for details of the finite-difference method)~~ are shown with dashed lines; each grid block is associated with material properties representing an important feature of the disposal system. These associations between grid blocks and material properties are shown by color and number in the figures. The two figures differ in that the material property map used for E1 intrusion events (Figure ~~6-14~~***6-15***) includes a material region representing the borehole (***Column 26*** ~~Region 1~~) that is not present in the undisturbed case ***(Figure 6-14)***. The borehole region vertically transects other material regions and connects the single panel (***Rows 10, 11, and 12*** ~~Region 23~~) with the Castile brine reservoir (***Rows 1 and 2*** ~~Region 30~~), marker beds, overlying units, and the surface. The E2 intrusion event material regions are similar to those of E1, except that the modeled borehole region does not extend below the repository and therefore does not contact a brine reservoir. ~~Additionally, the extent of the Castile brine reservoir is different from undisturbed to disturbed performance. This difference has no impact on results because no natural FEPs are retained that can create a pathway from the Castile to the repository.~~

Figures ~~6-13~~***6-14*** and ~~6-14~~***6-15*** show the relationship among material regions in the model and how connections are made within the finite-difference scheme. However, by illustrating equidimensional grid blocks, the volumetric relationship between grid blocks is greatly distorted. To show the volumetric relationship among nodal blocks and between the repository and host formations, a scaled side view of the vertical cross section used in BRAGFLO is shown in Figure 6-16. An undistorted 1:1 vertical:horizontal scale side view is in the upper left corner of Figure 6-16; at this scale, important model features are not resolvable. Therefore, two other views are provided in which the vertical scale has been exaggerated ~~50:1~~ to show model features. Notice that the modeling system extends ~~more than 15 miles (25 kilometers) to the north and~~ 14 miles ***(***22.***4***~~5~~ km ~~(14 mi)~~***) from the edge of the excavated repository in each direction, north and south. The borehole is not centered; rather it is located 24.17 km from the north boundary and 22.46 km from the south boundary.*** ~~to the south from the borehole, which intersects the approximate center of the waste disposal region and includes the uppermost 2,990 feet (911 meters) of rock at the WIPP site. Colors in Figure 6-14~~ ***Figure 6-16 colors*** are consistent with colors for material regions in Figures ~~6-13~~***6-14*** and ~~6-14~~***6-15***.

Effects of flow in the third (out-of-plane) dimension are approximated with a two-dimensional element configuration that simulates convergent or divergent flow to the north and south centered on the repository in intact rocks laterally away from the repository. ~~A top-down (plan) view of the model is shown in Figure 6-16 and illustrates the discretization adopted to simulate~~

~~convergent or divergent flow. Colors in Figure 6-16 are consistent with colors for material regions in Figures 6-13 through 6-15 at the repository depth (node rows 8, 9, and 10).~~ In this text, the term width corresponds to the x (lateral) dimension of nodes, thickness refers to the y (vertical) dimension, and depth refers to the z (out-of-plane) dimension. The effects of the grid assumptions on fluid flow processes in the Salado are discussed in Appendix ***PA, Attachment MASS, Section 4.1.*** ~~MASS (Section MASS.4 and MASS Attachment 4-1)~~

Based on observations in the existing excavations, the DOE approximates the regionally variable dip in the Salado by incorporating a 1-degree dip to the south in the BRAGFLO computational mesh. This dip is not indicated in Figures ~~6-13~~***6-14***, ~~6-14~~***6-15***, and ~~6-15~~***6-16***.

The BRAGFLO definition of hydrostratigraphic units follows formation and member divisions. Inside the Salado, however, further subdivision of hydrostratigraphy has been made based on the observed ~~in~~ permeability differences between anhydrite-rich interbeds and halite-rich intervals.

This further subdivision has been made only at elevations near the repository horizon, because only in this region are such distinctions important. The models and assumptions ~~used to~~ represent***ing*** the various regions of material properties shown in Figures ~~6-13~~***6-14*** and ~~6-14~~***6-15*** are discussed ~~beginning~~ in Section 6.4.3 and ~~in~~ Appendi***x PA, Section 4.2.*** ~~ces MASS and PAR.~~ The thickness of hydrostatigraphic units used in BRAGFLO are tabulated in Appendix PA~~R~~***, Attachment PAR, Table PAR-49.*** ~~(Table PAR-57).~~

6.4.2.2 Culebra Geometry

Although the BRAGFLO model contains a discretization of the Culebra and calculates flow there, the DOE uses a more detailed representation ~~of this unit~~ to estimate potential radionuclide releases to the accessible environment resulting from lateral subsurface transport ***through the Culebra***. The conceptual model for flow and transport in this geometry is discussed in Section 6.4.6.2. The boundary and initial conditions applied to this geometry are discussed in Section 6.4.10.2. ***MODFLOW-2000*** ~~SECOFL2D~~ and SECOTP2D are ~~the computer codes~~ used to simulate groundwater flow and radionuclide transport in the Culebra. ***The SECOFL2D code was used in the CCA to simulate groundwater flow and has been replaced with MODFLOW-2000. The groundwater flow and transport conceptual models have not changed; the implementation of the groundwater model has been updated.*** The manner in which this geometry is linked to the BRAGFLO geometry described in the preceding section is discussed in Sections 6.4.6.2, 6.4.11, and Appendix ***PA, Section 4.9.*** ~~CODELINK (Section CODELINK.6).~~ The grids used ~~for modeling~~ ***to model*** the Culebra are discussed in Section 6.4.6.2 ***and Appendix PA, Section 4.8 (see also Appendix PA, Attachments MASS and TFIELD).***

6.4.3 The Repository

The repository, as shown in Figure 3-2 ~~(see Chapter 3.0)~~, is represented by ***areas marked Waste Panel and rest of repository (RoR) north and south*** ~~Regions 23 to 27~~ in Figures ~~6-13~~***6-14*** and ~~6-14~~***6-15***. These regions include a waste disposal panel~~(Region 23)~~, panel closures (~~Region 25~~ ***DRF_PCS, CONC_PCS, Anhydrite AB, and DRZ_PCS***), ***two areas that represent*** the ***other*** panels and access drifts in the rest of the waste disposal region (~~Region 24~~ ***RoR north and***

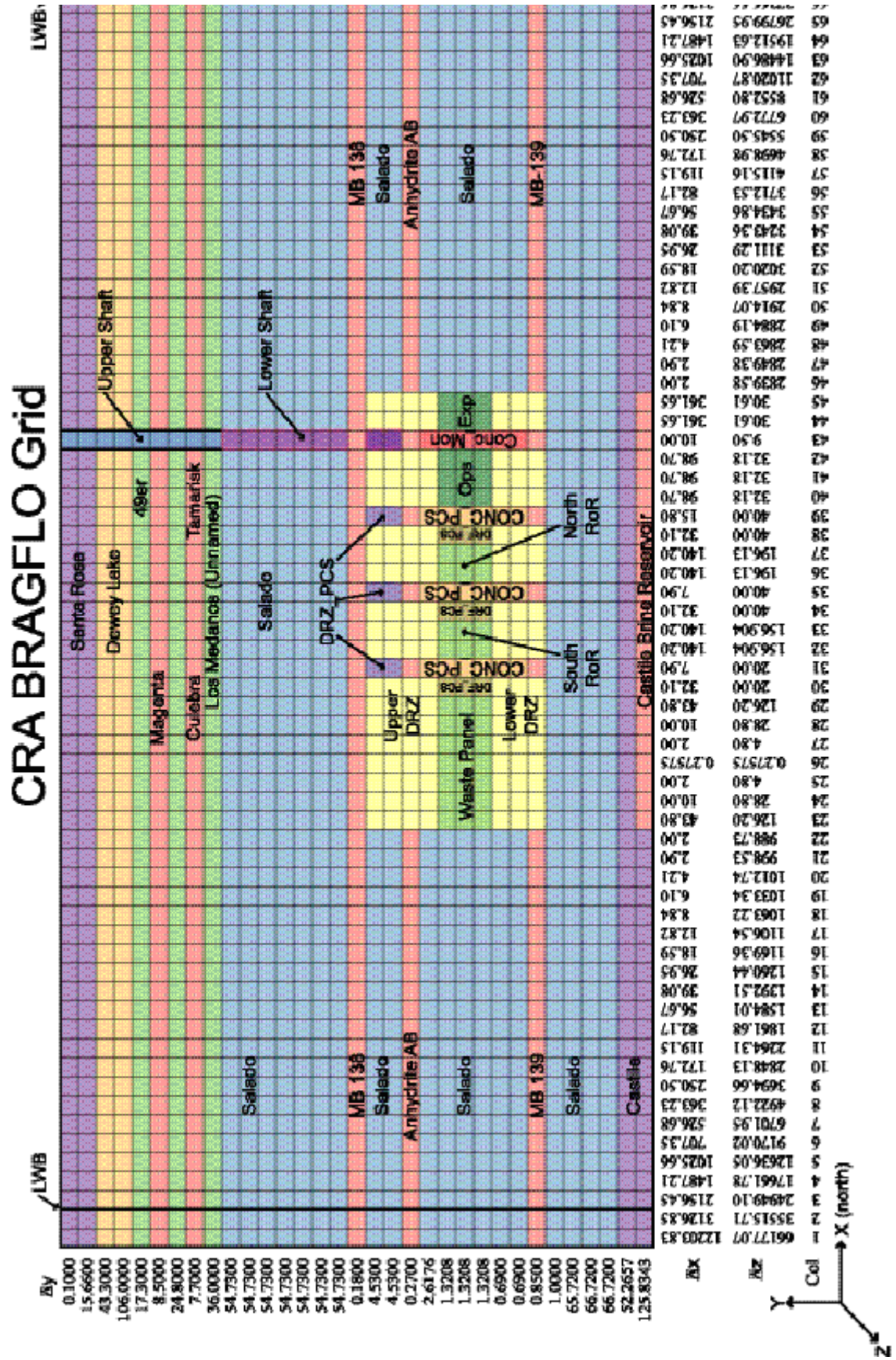

Figure 6-136-14. A Side View of the BRAGFLO Elements and Material Regions Used for Simulation of Undisturbed Performance

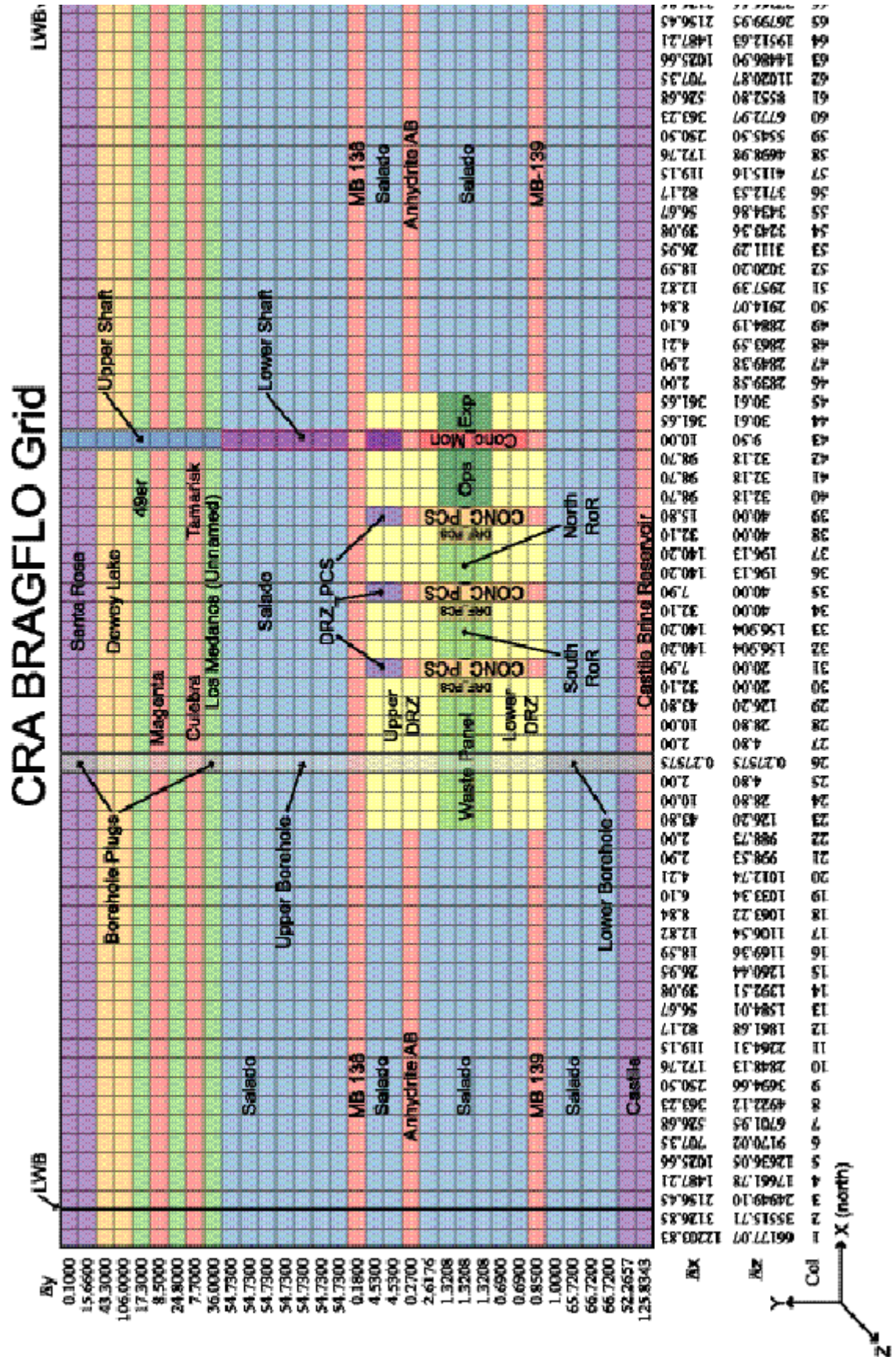

Figure 6-446-15. A Side View of the BRAGFLO Elements and Material Regions Used to Simulate the E1 Event

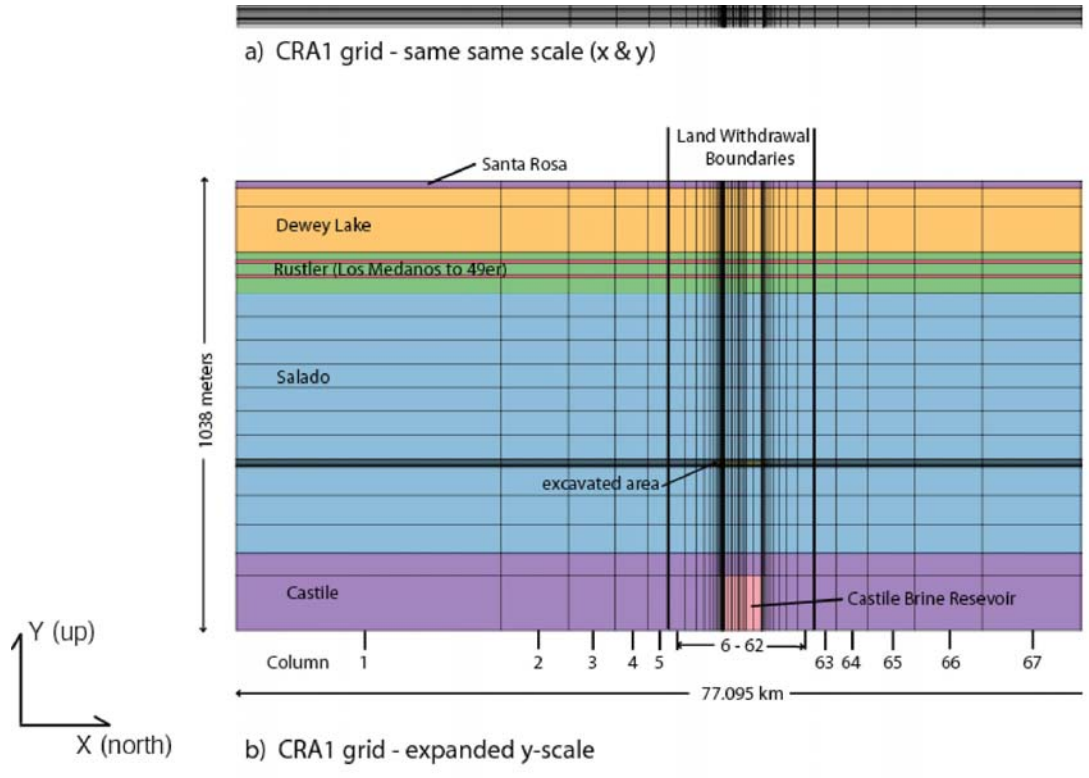

Figure ~~6-15~~*6-16*. A Side View of the BRAGFLO *CRA-2004* Geometry Drawn to Scale

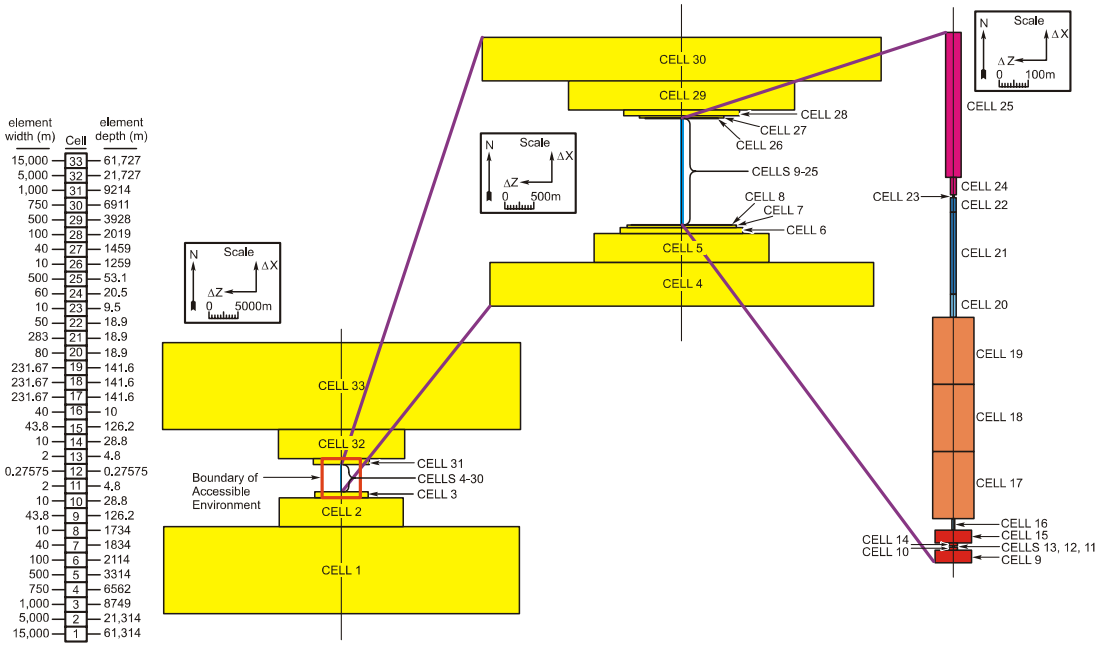

Note: This view illustrates the variation in element depth present in the model for simulation of radially convergent flow.

CCA-065-2

~~**Figure 6-16. A Top-Down View of a row of Elements in BRAGFLO Used for Undisturbed Performance**~~

south), the operations region (~~Region 26~~ *Ops*), and the experimental region at the north end of the repository (~~Region 27~~ *Exp*). The shaft ~~(Region 2~~ (which is further subdivided into *two primary regions marked Upper Shaft and Lower Shaft)* ~~Regions 3 through 11)~~ intersects the repository between the operations region and the experimental region. The shaft is discussed in ~~detail in~~ Section 6.4.4. For human-intrusion events, the borehole ~~(Region 1)~~ intersects the waste disposal region in the *P*~~p~~anel. In two-dimensional fluid flow codes, a grid block's length, volume, and cross-sectional area of faces connected to other grid blocks are important model features. For each region of the repository depicted, the BRAGFLO model geometry preserves the ~~true~~ excavated volume. Lateral dimensions have been determined to preserve volume and retain important cross-sectional areas and distances between defined regions, as discussed below. These simplifications are conservative with respect to fluid contact with waste, which is a critical factor in determining the quantity of actinides mobilized in the aqueous phase. The simplifications are conservative because (1) all pillars have been removed from the modeled panel, resulting in homogeneous waste regions through which fluid can flow directly; and (2) the panels in the rest of the repository *areas do not* have ~~neither~~ pillars~~nor closures~~, resulting in a large homogeneous region that is assigned an average permeability within the range of *those* experimentally determined ~~permeabilities~~ (see Section 6.4.3.2 and *Appendix PA*, ~~Appendix~~ *Attachment* MASS Section *3.1*~~MASS.5~~).

The single panel that is represented individually (*Panel* ~~Region 23~~) is discretized to simulate radial flow to and from the borehole that intersects it. *In the CCA grid, the distance from the borehole to the shaft was 1260 m (4133.8 ft), the true distance from the shaft to the south end of the waste disposal region. In the current grid, the distance is 1097 m (3599 ft). The distance was reduced during the re-gridding process that accounted for the Option D panel closures and refinements to represent two RoRs (see Appendix PA, Attachment MASS, Section 4.2.4).* ~~The true distance from the south end of the waste disposal region to the waste handling shaft is preserved in the model as the distance from the south end of the modeled panel to the modeled single shaft.~~ In BRAGFLO, the single panel region is the southernmost portion of the repository. It occupies this position because separate modeling activities indicate that slightly larger releases may result from a panel in this position than from alternative placements (see Vaughn et al. 1995).

Panel closures were originally represented generically, since there were four options for the panel closure design. A condition of the original WIPP certification requires the DOE to use the Option D panel closure design constructed with Salado Mass Concrete (SMC). The closure representation for this analysis is modified in the models to better represent the Option D panel closures (see Appendix PA, Section 4.2.8, Attachment MASS, and Chapter 9.0). The panel closure between the panel and the rest of the repository has a cross-sectional area equal to the cross-sectional area of the drifts between panels. The length and total volume of modeled panel closures is consistent with the~~ir~~ *Option D* design. The panel closure between the rest of the repository and the operations regions has a cross-sectional area equal to the cross-sectional area of the drifts between the north end of the waste disposal region and the operations regions. Because there are two closures between the waste disposal region and the shafts in the operations regions, the modeled panel closures between the rest of the repository and the operations regions have a length and volume consistent with two panel closures.

A number of submodels have been defined within the repository region and are described in this section. The submodels that have been defined for repository processes are Creep Closure (6.4.3.1), Repository Fluid Flow (6.4.3.2), Gas Generation (6.4.3.3), Chemical Conditions in the Repository (6.4.3.4), Dissolved Actinide Source Term (6.4.3.5), and Source Term for Colloidal Actinides (6.4.3.6).

6.4.3.1 Creep Closure

Salt creep occurs naturally in the Salado halite in response to deviatoric stress. Inward creep of rock and the repository response is ~~a process~~ generally referred to as creep closure. Creep closure of excavated regions begins immediately because of excavation-induced deviatoric stress. If the rooms were empty, closure would proceed to the point where the void volume created by the excavation would be eliminated as the surrounding formation returns to a uniform stress state. In the waste disposal region, waste consolidation ~~will~~ continue***s*** until loading in the surrounding rock is uniform, at which point salt creep ***and waste consolidation*** ceases. The amount of waste consolidation that occurs and the time it takes to consolidate are governed by properties of the waste (waste strength, modulus, etc.), properties of the surrounding rock, the dimensions and location of the room, and the quantities of fluids present ~~in the room~~.

Fluids that could affect closure are brine that may enter the repository from the Salado or an intrusion borehole, air present in the repository when it is sealed, and gas produced by reactions occurring during waste degradation. Closure and consolidation can be slowed by fluid pressure in the repository. This can be quantified according to the principle of effective stress:

$$\sigma_T = \sigma_e + p \,, \qquad (6.11)$$

where σ_T is the stress caused by the weight of the overburden (an essentially constant value), p is the pressure of the repository pore fluid, and σ_e is the stress ~~that is~~ applied to the waste matrix. In this formulation, the waste is considered a skeleton structure containing pore fluids. As the pore pressure increases, an increasing amount of overburden stress is supported by pore fluid pressure, p ~~p~~, and less overburden stress is supported by the strength of the waste matrix. Waste consolidation will cease when the sum of the stresses felt by the waste matrix and fluid pressure reaches lithostatic pressure. If gas and brine quantities in the repository stabilize, creep closure will act to establish a constant pressure and pore volume.

In summary, creep closure of waste disposal areas will cause their volume to decrease as the Salado deforms to consolidate and encapsulate the waste, changing waste porosity and permeability. Resistance to creep closure will be caused by waste strength and fluid pressure.

Three major material-response models are required for closure analyses. The first model describes how the halite creeps as a function of time and stress. The second model describes the state of ~~consolidation of the~~ waste ***consolidation*** as a function of applied stress. A third constitutive model is used to model inelastic behavior of anhydrite marker beds (see Appendix ***PA, Attachment MASS, Section 13.0*** ~~PORSURF, PORSURF Attachment 1~~).

Halite deformation is predicted using a multimechanism deformation steady-state creep model with work hardening and recovery transient response. For the conditions of the WIPP, creep

mechanisms are governed by the temperature and shear stress at a given location in the surroundings at any time. Although WIPP conditions are expected to be nearly isothermal at the ambient natural underground temperature, several ~~of the~~ mechanisms can be active at the same time because of the large range of stress states that occur around underground rooms and shafts. The focus of the ***model's*** mechanistic part ~~of the model~~ is definition of steady-state creep strain, with transient creep strain described through a multiplier on the steady-state rate, thus accommodating both transient changes in stress loading and unloading.

The volumetric plasticity model is the mathematical model for room closure and waste consolidation. The ***model is discussed further and the*** experimental data used in this model are summarized and interpreted in ***Butcher and Mendenhall (1992),*** Butcher et al. (1991, 65-76) ***and*** Luker et al. (1991).

The volumetric plasticity model, multimechanism deformation model, and the inelastic constitutive model for anhydrite were numerically implemented in the SANTOS computer code to calculate the closure of disposal rooms for ~~performance assessment~~***PA*** (Appendix ***PA, Attachment PORSURF***. ~~PORSURF, PORSURF Attachment 1). SANTOS is described in Appendix PORSURF (Section PORSURF.3~~)

As a boundary condition, SANTOS requires ~~estimates of the~~ fluid pressure ***estimates*** and hence the quantity of gas present in a disposal room. These estimates are obtained using the average stoichiometry model of gas generation (Section 6.4.3.3) with different rates of gas generation that reflect different assumptions about the quantity of brine ~~that might be~~ available in a waste disposal room. The different rates of gas generation used in SANTOS bound the possible conditions for gas content in the repository. With the volumetric plasticity model and the fluid pressure boundary condition, SANTOS calculates the pore volume of the disposal room through time.

In ~~performance assessment~~***PA***, ***SANTOS calculates*** the time-dependent effects on volume ***as a result*** of creep closure***.*** ~~calculated by SANTOS~~ ***These effects*** are linked to the fluid-flow code BRAGFLO by a porosity surface, which is a look-up table relating porosity (void volume) to (1) time after sealing and (2) gas pressure. At the beginning of a time step, BRAGFLO evaluates the pressure of a cell in the waste disposal regions; the pressure is sensitive to brine and gas flow and the previous pore volume of the cell. The code then consults the porosity surface to find the appropriate void volume of the cell for a given time and pressure. The void volume in the cell is iteratively adjusted during a time step for consistency with gas generation, fluid movement, and repository pressure. Additional details about the porosity surface method are included in Appendix ***PA, Attachment PORSURF.*** ~~BRAGFLO (Section 4.11) and Appendix PORSURF (Sections PORSURF.1, PORSURF.2, and PORSURF Attachments 1 through 6).~~ The porosity surface method of incorporating the ~~dynamic effect of~~ creep closure***'s dynamic effect*** in ~~performance assessment~~***PA*** has been compared to more complex techniques that are computationally impractical in a ~~performance assessment~~***PA*** (Freeze et al. 1995). In these comparisons, the porosity surface method was found to ~~be a reasonable representation of~~ ***reasonably represent*** behavior observed in more complex models.

The operations area and experimental area (***Columns 40 to 45*** ~~Regions 26 and 27~~ in Figures 6-14 and 6-15~~, respectively~~) are modeled as unfilled after closure in this ~~performance assessment~~***PA***.

The operations and experimental areas ~~These regions~~ are expected to close in less than 200 years and do not require a porosity surface, in contrast to the region containing waste (Vaughn et al. 1995). ***These areas are assumed to be "pre-closed" and are assigned a constant low porosity (18 percent) over the entire regulatory time frame.***

Additional modeling confirmed that new waste types (compacted waste forms) and waste containers (pipe overpacks) do not impact the adequacy of the original porosity surface modeled in the CCA PA. The porosity surface used in the CCA is used in this analysis.

6.4.3.2 Repository Fluid Flow

Fluid flow modeling within the repository is concerned with (1) fluid flow and distribution in the waste, (2) fluid flow to and from the Salado and shafts, and (3) fluid flow between the repository and intrusion boreholes. These are important in assessing gas generation rates (Section 6.4.3.3), repository pressure, and the mobility of radionuclides in the disposal system. Additional discussion of this topic is provided in ***Appendix PA,*** ~~Appendix,~~ ***Section PA-4.2.*** ~~MASS (Section MASS.7).~~

Disposal region fluid flow is affected by the geometrical association of pillars, rooms, drifts, panel closures, possible borehole locations, ~~the~~ time-dependent properties of waste areas resulting from creep closure, flow interactions with other parts of the disposal system, and reactions that generate gas. As described in Section 6.4.3.1, creep closure changes disposal region porosity. Depending on material properties and conditions, brine may flow into the disposal region ~~by moving down shafts and~~ through the DRZ ~~or operations region~~, or, during disturbed conditions, through a borehole. Brine contained in the Salado may flow to the waste disposal region because of pressure gradients created by the excavation. Brine flow into the repository may be reduced as repository pressure increases, and brine may be expelled from the repository if pressure in the repository exceeds brine pressure in the immediately surrounding rock or borehole. Gas may be generated as waste decomposes, causing a pressure increase. Gas may flow away from the waste ***area to the anhydrite marker beds by hydrofracturing processes in the DRZ and anhydrite interbeds.*** ~~into lower pressure areas, which may include disturbed areas surrounding the repository, the interbeds, the shafts, or an intrusion borehole.~~ Gas flow into intact, halite-rich rock is not expected because of the expected high threshold pressure of halite (see Section 6.4.5.1).

Fluid flow in the disposal system is conceptualized using principles of multiphase flow, except for Culebra flow and transport modeling. In multiphase flow, a residual brine saturation (S_{br}), is defined, which is the minimum saturation at which the brine phase has a nonzero relative permeability; below this saturation, brine is immobile. In accordance with two-phase flow theory, the residual gas saturation (S_{gr}) in the disposal system corresponds to the gas saturation necessary to create an incipient gas-phase relative permeability; below this saturation, waste-generated gas is immobile. The multiphase flow techniques adopted by the DOE are described in ***Appendix PA, Section 4.2 and Attachment MASS, Section 3.0.*** ~~Appendix BRAGFLO (Section 4.8).~~

The intrinsic permeability of waste at a given time can influence repository system performance by affecting the flow rate of gas or brine through the waste. Tests reported by Luker et al. (1991,

693-702) on simulated waste have shown material permeabilities ~~from about~~ ***of*** 10^{-12} to 10^{-16} m^2 on waste compacted under a lithostatic load. ~~Performance assessment~~***PA*** assigns ~~a~~ ***waste*** permeability ~~of the waste~~ as a constant at ***2.4*** ~~1.7~~ × 10^{-13} m^2 (~~Table 6-8~~ ***Table 6-10***). This permeability value ***was adopted from the value used in the PA verification test (EPA 1998, TSD V-B-14).*** ~~is representative of the average value of compacted waste. Use of a constant value rather than a variable has been found acceptable (Vaughn et al. 1995).~~

Because two-phase relationships have not been measured for waste, ~~performance assessment~~***PA*** determines a range of possible two-phase conditions for the repository by applying the LHS technique to parameters within the Brooks-Corey two-phase equations. These and other parameters in the disposal room and repository flow model are shown in Tables ~~6-8~~***6-10*** and ~~6-9~~***6-11***. Details about the two-phase equations and parameters used in ~~performance assessment~~***PA*** are included in Appendix ***PA, Section 4.2; Attachment MASS, Section 3.0;*** ~~BRAGFLO (Sections 4.8 and 4.9)~~ and ***Attachment*** ~~Appendix~~ PAR (Parameters 6 and 7).

Material properties in the waste are assumed to be homogeneous and are distributed in the BRAGFLO model ~~in~~ ***to*** cells whose volumes are much larger than an individual waste container.

Two processes that may occur on scales smaller than the cell volumes in BRAGFLO are wicking (the retention of brine in a capillary fringe) and puddling (the capture of brine in isolated pockets of waste caused by waste heterogeneity). Wicking is accounted for in the gas generation model (Section 6.4.3.3). Vaughn et al. (1995) found that puddling can be neglected.

The experimental and operations regions (***Columns 44 and 45 and 40 through 42, respectively,*** ~~Regions 26 and 27~~ in Figures 6-14 and 6-15) are represented in ~~performance assessment~~***PA*** with a porosity of 18 percent and a permeability of 10^{-11} m^2 as a conservative upper bound. For postoperational performance, the panel closures (***Columns 31, 35, and 39*** ~~Region 25~~ in Figures 6-14 and 6-15) are represented with a porosity of ***5*** ~~7.5~~ percent and a ***median*** permeability of ***1.78×10^{-19}*** ~~10^{-15}~~ m^2, as discussed in ~~Appendix MASS (MASS Attachment 7-1)~~ ***Appendix PA, Section 4.2, Attachment PAR, Parameter 10, and Attachment MASS, Section 19.0.***

6.4.3.3 Gas Generation

Gas will be produced in the repository ***by*** ~~because of~~ a variety of chemical reactions, primarily those occurring ***among*** ~~between~~ brine, metals, microbes, cellulosics~~,~~ ***,*** ~~and similar materials,~~ plastics~~,~~, and rubber materials, and ~~via liberation~~ ***release***~~s~~ of the dissolved gases ***produced by these reactions to the gaseous*** ~~to the gas~~ phase. The dominant processes are anoxic corrosion of ~~metals~~ ***steels and other Fe-based alloys*** in the waste containers, and the waste and microbial ***consumption*** ~~degradation~~ of cellulosics~~,~~, plastics~~,~~, and rubbers~~ ~~ ***materials*** ~~in the waste~~. Anoxic corrosion ***of steels and other Fe-based alloys*** ~~reactions will occur between brine and steel,~~ ***and*** ~~aluminum~~***Al,*** and ~~aluminum~~ ***Al-base*** alloys~~, producing~~ ***by water in the brine will occur, producing H_2.*** Microbial ~~degradation~~ ***consumption*** of cellulosics~~,~~ ***, plastic, and rubber materials could*** ~~may~~ produce a variety of gases; however, for the ***current*** waste inventory ~~and expected conditions~~, CO_2 and CH_4 ~~(methane)~~ are expected to ~~be~~ ~~the~~ dominate ***(as predicted at the time of the CCA).*** ~~gases for the process.~~ Radiolysis ~~has been~~ ***was*** demonstrated by laboratory experiment and model calculations to be insignificant (see ~~Appendix MASS, Section MASS.8;~~ ***Appendix PA, Attachment SCR, FEP W15 and W53).*** ~~Appendix SCR, Section SCR.2.5.1.3).~~

Table *6-10*~~6-8~~. Repository[a 1] and Panel Closures Parameter Values

Parameter (units)	Maximum	Minimum	Median or Constant
Permeability, k (square meters) – Waste Region	–	–	*2.4*~~1.70~~ × 10^{-13}
Permeability, k (square meters) – Operations and Experimental Regions	–	–	10^{-11}
Permeability (square meters) – Panel Closures	*1 × 10^{-17}*	*2.00 × 10^{-21}*	*1.78 × 10^{-19}* ~~10^{-15}~~
Initial Effective Porosity (percent) – Waste Region	–	–	84.8
Effective Porosity (percent) – Operations and Experimental Regions	–	–	18.0
Effective Porosity (percent) – Panel Closures	–	–	*5* ~~7.5~~
Threshold Pressure, P_t (pascals) – Repository[a 1]	–	–	0
Threshold Pressure, P_t (pascals) – Panel Closures[b 2]	–	–	*1.72 × 10^6* ~~8.67 × 10^4~~
Residual Brine Saturation, S_{br} (unitless) – Repository	0.552	0	0.276
Residual Brine Saturation, S_{br} (unitless) – Operations and Experimental Regions	–	–	0
Residual Brine Saturation, S_{br} (unitless) – Panel Closures	*0.60*	*0*	0.20
Residual Gas Saturation, S_{gr} (unitless) – Repository	0.15	0	0.075
Residual Gas Saturation, S_{gr} (unitless) – Operations and Experimental Regions	–	–	0
Residual Gas Saturation, S_{gr} (unitless) – Panel Closures	*0.40*	*0*	0.20
Pore Distribution Parameter, λ (unitless) – Repository	*5.78*	*1.44*	2.89
Pore Distribution Parameter, λ (unitless) – Operations and Experimental Regions	–	–	0.7
Pore Distribution Parameter, λ (unitless) – Panel Closures	*8.10*	*0.11*	0.94
Maximum Capillary Pressure (pascals) – Repository and Panel Closures	–	–	10^8
Pore Compressibility (1/pascals) – Repository[c 3]	–	–	0
Pore Compressibility (1/pascals) – Panel Closures	–	–	~~2.64 × 10^{-9}~~ *6 × 10^{-11}*

[a 1] Unless specifically listed, Repository refers to operations, experimental, and waste regions.

[b 2] Threshold pressure (P_t) determined from the relationship: $P_t = PCT\_A \cdot k^{PCT\_EXP}$ where PCT_A and PCT_EXP are constants and k is the permeability.

[c 3] Accounted for in porosity surface.

Gas generation will affect repository pressure, which is important in other submodels of the disposal system, such as those calculating creep closure (Section 6.4.3.1), interbed fracturing (Section 6.4.5.2), two-phase flow (Section 6.4.3.2), and the radionuclide release*s* associated with spallings during an inadvertent drilling intrusion (Section 6.4.7). Thus, gas generation must be estimated in ~~performance assessment~~*PA*.

Table *6-11*~~6-9~~. BRAGFLO Fluid Properties

Parameter (units)	Value
Reference Temperature (kelvin)[a] *1*	300.15
Liquid Density (kilograms per cubic meter)[a,b] *1,2* at	
Atmospheric Pressure	1,220.0
8 megapascals	1,223.0
15 megapascals	1,225.7
Liquid Viscosity (pascals * seconds)[b] *2*	2.1×10^{-3}
Liquid Compressibility (1/pascals)[b] *2*	3.1×10^{-10}
Gas Density (kilograms per cubic meter)[a,b] *1,2* at:	
Atmospheric Pressure	0.0818
8 megapascals	6.17
15 megapascals	11.1
Gas Viscosity (pascals * seconds)[b] *2*	8.93×10^{-6}

[a] *1* These values applied to fluids in all material regions in BRAGFLO.

[b] *2* See Appendix *PA* ~~BRAGFLO~~ (Section *4.2*~~4.4~~) for equations of state.

~~Performance assessment~~*PA* uses the average~~-~~stoichiometry model to estimate gas generation occurring in the waste~~-~~disposal region. This model was developed for WIPP ~~performance assessment~~*PA* based on gas~~-~~generation experiments performed for the WIPP **(**see *CCA* Appendix MASS, Section MASS.8 and MASS Attachment 8-2**)**. The average~~-~~stoichiometry model accounts for ~~the formation of~~ gas *formed* by anoxic corrosion of steels *and other Fe-based alloys,* and microbial *consumption* ~~degradation~~ of cellulosic~~s~~, ~~including~~ plastic~~s~~, and rubber~~s~~ *materials*. For ~~the purpose of~~ calculating repository pressure and gas flow, the density and viscosity of the generated gas are assumed to be those of H_2. In the average~~-~~stoichiometry model, gas is assumed to be generated at a rate dependent on the availability of brine in the computational cell. Gas can be generated by anoxic corrosion in all realizations, and is assumed to be generated by microbial *activity* ~~degradation~~ in half of the realizations. The average~~-~~stoichiometry model is based on experimental data on the rates of *gas generation from anoxic* corrosion *of steels* and microbial *consumption* ~~degradation~~ *of papers* under inundated and humid conditions. These data were used to develop ranges of possible gas-generation rates, as shown in ~~Table 6-10~~ *Table 6-12*. In BRAGFLO, a gas-generation rate is determined from the rates listed in ~~Table 6-10~~ *Table 6-12* by a linear-interpolation method that combines humid and inundated rates based on the effective liquid saturation (Appendix *PA* ~~BRAGFLO~~, Section *PA-4.2.5* ~~4.13~~).

The effective liquid saturation in a computational cell ~~in~~ *of* BRAGFLO for the purpose of gas generation is the computed liquid saturation in that cell plus an adjustment ~~to account~~ for uncertainty in the capillary rise (wicking) characteristics of the waste. Refer to *Attachment PA,* Sections *PA-4.2.5 and PA-4.2.6* ~~4.13 and 7.2.9~~, *Attachment* ~~Appendices~~ PAR (Parameter 8) ~~and BRAGFLO~~ for details on the treatment of wicking in the gas~~-~~generation model.

Anoxic corrosion is represented by a generic equation given in Appendix *PA* ~~BRAGFLO~~ (Section *PA-4.2.4* ~~4.13~~). This equation accounts ~~for corrosion~~ only *for corrosion of* ~~the~~ steel*s and other Fe-based alloys* ~~content~~ in the repository by the reaction expected to dominate.

Table *6-12*~~6-10~~. Average-Stoichiometry Gas Generation Model Parameter Values

Parameter (units)	Maximum	Minimum	Median or Constant
Inundated Corrosion Rate for Steel without CO_2 Present (meters per second)	*3.17×10^{-14}* ~~1.59×10^{-14}~~	0	*1.59* ~~7.94×10^{-15}~~
Humid Corrosion Rate for Steel	–	–	0
Probability of Microbial *Consumption* ~~Degradation~~ of Plastic~~s~~ and Rubber~~s~~ *Materials* in the Waste in the Event of Significant Microbial Gas Generation (see Figure PAR-1) where 0 represents corrosion and no significant microbial gas generation. 1 represents cellulosic degradation only, and 2 represents cellulosic, plastic, and rubber ~~degradation~~*consumption*	2	0	2
Rate for Microbial *Activity* ~~Degradation~~ Under Humid Conditions (mole per kilogram $*$ second)	1.27×10^{-9}	0	6.34×10^{-10}
Rate for Microbial *Activity* ~~Degradation~~ under Brine-Inundated Conditions (mole per kilogram $*$ second)	9.51×10^{-9}	3.17×10^{-10}	4.92×10^{-9}
Factor β for Microbial Reaction Rates (unitless)	1.0	0	0.5
Anoxic Corrosion Stoichiometric Factor X (unitless)	–	–	1.0
Average Density of Cellulosic~~s~~ *Materials* in CH-TRU Waste (kilograms per cubic meter)	–	–	*58* ~~54.0~~
Average Density of Cellulosic~~s~~ *Materials* in RH-TRU Waste (kilograms per cubic meter)	–	–	*4.5* ~~17.0~~
Average Density of ~~Iron~~*Steels and Other Fe*-Based ~~Materials~~*Alloys* in CH-TRU Waste (kilograms per cubic meter)	–	–	*110.0* ~~170.0~~
Average Density of ~~Iron~~*Steels and Other Fe*-Based ~~Materials~~*Alloys* in RH-TRU Waste (kilograms per cubic meter)	–	–	*110.0* ~~100.0~~
Average Density of Plastic~~s~~ *Materials* in CH-TRU Waste (kilograms per cubic meter)	–	–	*42.0* ~~34.0~~
Average Density of Plastic~~s~~ *Materials* in RH-TRU Waste (kilograms per cubic meter)	–	–	*4.9* ~~15.0~~
Average Density of Rubber *Materials* in CH-TRU Waste (kilograms per cubic meter)	–	–	*14.0* ~~10.0~~
Average Density of Rubber *Materials* in RH-TRU Waste (kilograms per cubic meter)	–	–	*3.1* ~~3.3~~
Bulk Density of ~~Iron~~*Steel* Containers, CH-TRU Waste (kilograms per cubic meter)	–	–	*170.0* ~~139.0~~
Bulk Density of ~~Iron~~*Steel* Containers, RH-TRU Waste (kilograms per cubic meter)	–	–	*480.0* ~~2.59×10^{3}~~
Bulk Density of Plastic Liners, CH-TRU Waste (kilograms per cubic meter)	–	–	*16.0* ~~26.0~~
Bulk Density of Plastic Liners, RH-TRU Waste (kilograms per cubic meter)	–	–	*1.4* ~~3.1~~
Total Volume of CH-TRU Waste (cubic meters)	–	–	1.69×10^{5}
Total Volume of RH-TRU Waste (cubic meters)	–	–	7.08×10^{3}
Wicking Saturation (unitless)	1.0	0	0.5

Because the total quantity of ~~aluminum~~*Al* and ~~aluminum~~ *Al-base* alloys is ~~a~~ small compared to the quantity of ~~iron~~*steels and other Fe*-base*d* ~~metals~~*alloys*, corrosion of ~~aluminum~~*Al* is omitted for simplicity. The steel*s and other Fe-based alloys are* ~~content of the repository is~~ depleted separately in each computational cell (that is, a cell-by-cell basis), and gas generation can continue in cells, depending on parameter values, until all *the* steel*s and other Fe-based alloys* ~~in a cell is~~ *are* consumed. Brine in cells is consumed as gas generation proceeds. If a cell has a brine saturation equal to zero, it cannot produce gas by anoxic corrosion.

It is assumed ~~that~~ there is no passivation ~~of anoxic corrosion~~ of steel*s or other Fe-based alloys* by CO_2 and H_2S produced by microbial *activity* ~~degradation~~ because microbial gas generation is too slow and also because CO_2 will be removed from the gaseous phase by ~~reaction with~~ *reacting with* MgO ~~backfill~~. Details of the equations and parameter values are given *in Appendix PA,* ~~and~~ *Attachment PAR (Parameters 1 through 5) and Appendix BARRIERS.* ~~Appendix BRAGFLO (Section 4.13), Appendix PAR (Parameter 1), and Appendix MASS (Section MASS.8.~~

Microbial ~~degradation~~ *activity* occurs in only half ~~of~~ the realizations because of uncertainties *associated with* ~~in viability of the colonies~~ *this process* (Appendix *PA, Attachment* MASS, Section ~~MASS.~~8*.0* ~~and MASS Attachment 8-2~~). Like anoxic corrosion, microbial ~~degradation~~ *gas production* is represented by a generic equation, given ~~along~~ with other details in Appendix *PA* ~~BRAGFLO~~ (Section *4.2.5*~~4.13~~). The ~~cellulose~~ inventory *of cellulosic, plastic, and rubber materials* is depleted on a cell-by-cell basis. Depending on parameter values, gas generation by microbial ~~degradation~~ *activity* can continue until all cellulosic~~s~~ *materials* in the cell are degraded. Reaction with ~~MgO added to the repository~~ *the MgO engineered barrier* consumes CO_2 (see Section 6.4.3.4 and *Appendix PA, Attachment* ~~Appendix~~ SOTERM~~, Section SOTERM.2.2.2~~). Thus, the net quantity of gas ~~produced~~ *developed* by microbial ~~degradation~~ *consumption of cellulosic, plastic, and rubber materials* is correlated with constituents of the waste disposal region. ~~Details are provided in Appendix BRAGFLO (Section 4.13).~~ It is assumed that microbial ~~degradation process~~ *activity* neither produces nor consumes water, but its rate is dependent on the amount of liquid present in a computational cell.

Microbi~~al~~*es* ~~degradation~~ may *also* consume plastic and rubber materials in the repository. The DOE assumes that in half of ~~those~~ *the* simulations ~~in which~~ *where* microbial *consumption* ~~degradation~~ of cellulosic~~s~~ *materials* occurs, microb*es*~~ial degradation~~ also ~~acts on~~ *consume* plastic and rubber materials in the waste-disposal region. As with cellulosic~~s~~ *materials*, these *plastic and rubber* materials are depleted on a cell-by-cell basis. Parameter values for the average-stoichiometry model are summarized in ~~Table 6-10~~*Table 6-12* and detailed in Appendix *PA, Attachment* PAR (Parameters 1 through 5).

6.4.3.4 Chemical Conditions in the Repository

The chemical conditions in the repository determine actinide solubilit~~y~~*ies*, ~~a property~~ *parameters* demonstrated in past analyses as important to disposal-system performance. In scenarios ~~that have~~ *with* the potential to ~~result~~ *cause* ~~in~~ releases to the accessible environment, the DOE has determined that chemical conditions ~~in the repository~~ can be modeled *in PA* as *homogeneous throughout the waste-disposal area and* constant *(with the exception of brine content) throughout the 10,000-year regulatory period.* ~~in performance assessment.~~ This use of

constant***, homogeneous*** conditions is based on ~~an~~ ***the*** assumption of equilibri***a***~~um~~ ***(***for most processes***)*** ~~between the~~ ***among*** brine ***(the composition of which is determined by the scenario being considered),*** ~~in the repository (determined by the scenario being considered), waste, MgO backfill, and abundant~~ minerals ***that are abundant in the Salado, the MgO engineered barrier, and the actinides in the waste***. Some exceptions to ~~the~~***this*** ~~equilibrium~~ assumption ~~of equilibria~~ are present in ~~some~~ performance~~-~~assessment models and are discussed where appropriate. In addition to the following discussion, information supporting this position is presented in Appendix ***PA, Attachments*** SOTERM ***and BARRIERS.***

Brine and waste within the WIPP repository are modeled as a ~~uniform~~ ***homogeneous*** mixture of dissolved and solid-state species. Thermodynamic equilibrium is assumed for dissolved actinide concentrations, but oxidation-reduction reactions between the actinides and other waste components are not assumed to ~~proceed to~~ ***reach*** equilibrium. Although materials in the waste will actually dissolve at different rates, the ***assumption of instantaneous solubility equilibria and*** ~~presumption of~~ homogeneity ~~and solubility equilibrium~~, along with assumed disequilibrium ~~reduction~~-oxidation***-reduction*** conditions, yields the largest reasonable concentration of ~~aqueous~~ ***dissolved and colloidal*** actinides in the repository. No chemical microenvironments that influence the overall chemical environment are expected to persist, nor is supersaturation expected during the 10,000-year regulatory period. The average temperature of the WIPP is expected to increase by less than ~~6~~***10***°C ***from its ambient value of 28°C*** as a result of radioactive decay and exothermic reactions, such as MgO hydration and carbonization, and the effect of this small increase is assumed negligible (see ***Appendix PA, Attachment SCR, FEPs W72 and W73).*** ~~Appendix WCA, Section WCA.5.3, and Appendix SCR, Sections SCR.2.2.2 and SCR.2.5.7).~~

Brine composition in the repository can vary depending on the sequence of future human events. Calculating ~~of~~ brine mixing from different sources is not ***feasible in*** ~~amenable to performance assessment~~***PA***. The DOE has made the reasonable simplification that in the undisturbed performance and E2 scenarios, which do not include penetration of a Castile brine reservoir, all brine in the repository will have the composition of Salado brine (see ***Appendix PA,*** ~~Appendix~~ ***Attachment*** SOTERM ~~Section SOTERM.2.2.1~~). In these scenarios, there is no process that could introduce Castile brine into the repository. For the E1 and E1E2 scenarios, which include penetration of a brine reservoir in the Castile, brine in the repository is assumed to have the composition of Castile brine at all times. Even though some Salado brine may enter the repository in these scenarios, it is reasonable to assume that Castile brine ~~is the~~ dominan~~t~~***es*** ~~portion of brine~~ because the quantity of brine that can flow from a reservoir through a borehole and into the repository is substantial compared to the quantity of brine entering from the Salado.

The chemical environment in the repository after closure is expected to be ***strongly*** reducing (that is, lowered oxidation states are expected ***for elements that can occur in more than one oxidation state*** ~~to be favored~~). Any gaseous or dissolved oxygen present in the repository will be consumed quickly either by aerobic microbe~~s~~***ial activity*** or by oxic corrosion after repository closure. Moreover, the repository will contain large amounts of ***metallic*** ~~iron~~***Fe***, and anoxic corrosion has been shown to produce considerable quantities of ~~hydrogen gas~~H_2, ~~and Fe^{2+}~~ ***Fe(II) oxides and hydroxides, and dissolved Fe(II) species*** under expected repository conditions (see Appendix MASS, MASS Attachment 8-3 ***of the CCA***). Despite the overall reducing conditions, however, a condition of ~~reduction~~-oxidation***-reduction*** disequilibrium is assumed in that

~~reduction~~ oxidation***-reduction*** reactions between dissolved actinides in possible oxidation states are ***not*** assumed to ~~not~~ occur.

~~Based on experimental data reported in AppendixSOTERM (Sections SOTERM.2.2.2, SOTERM.3.4, and SOTERM.3.6), the DOE has determined that alkaline conditions in the repository favor lower actinide solubility. As discussed in Section 3.3.3 andAppendix BACK MgO will be emplaced in the repository with the waste, in order to ensure alkaline conditions in the repository. MgO emplaced with the waste will react with the CO2 that forms, creating magnesium carbonate minerals such as MgCO3. The fugacity of CO2 will be low and controlled by equilibrium considerations, rather than controlled by its rate of production by microbial degradation, because the DOE will emplace enough MgO with sufficient surface area to ensure CO2 uptake will exceed the CO2 production rate. Thus, by adding MgO to the repository, the DOE not only maintains alkaline conditions but also minimizes a property of the repository, its CO2 fugacity, that would be expected to vary with time and potentially complicate the estimation of actinide solubilities in performance assessment.~~

~~MgO reacts with brine to form Mg(OH)2. Mg(OH)2 will react with CO2 produced by the microbial degradation of cellulosics by reactions such as~~

~~$$Mg(OH)2 + CO2 = MgCO3 + H2O \quad (12)$$~~

~~There is a small amount of other alkaline components in the waste, such as Ca(OH)2, contained in the cementitious waste. Their effect will be minimal because they will be consumed by reactions with MgCl2 in the Salado brine and microbially generated CO2. Details of those buffering reactions are described inAppendix SOTERM (Section SOTERM.2.2.2).~~

~~Because the processes that might cause time-dependent changes in important chemical conditions in the repository have been eliminated by the addition of MgO and by the assumptions made regarding brine composition, performance assessment uses constant chemical conditions. The chemical conditions in the repository, including the pmH (the −log10 of the molality of the hydrogen ion), are assumed to be controlled by equilibrium between minerals (that is, MgO, Salado halite, and anhydrite present in interbeds), brine present, and waste. In Salado brine, the pmH in this system will be about 9.4. In Castile brine, the pmH in this system will be about 9.9. In both systems, the carbon dioxide fugacity will be low and will be determined by the equilibrium system (seeAppendix SOTERM, Section SOTERM.2.2.2, for a detailed discussion).~~

MgO in polypropylene "supersacks" is emplaced on top of the three-layer waste stacks to create conditions that reduce actinide solubilities in the repository (see Section 3.3.3; Appendix BARRIERS; and Appendix PA, Attachment SOTERM, Section SOTERM-2.0). If brine flows into the repository, MgO will react with water in brine and in the gaseous phase to produce brucite ($Mg[OH]_2$). MgO will react with essentially all of the CO_2 that could be produced by complete microbial consumption of the cellulosic, plastic, and rubber materials in the waste, and will create hydromagnesite with the composition $Mg_5(CO_3)_4(OH)_2{\cdot}4H_2O$ (Appendix BARRIERS; Appendix PA, Attachment SOTERM, Section 2). The most important MgO hydration and carbonation reactions that will occur in the WIPP are:

$$MgO + H_2O(aq\ and/or\ g) \rightleftharpoons Mg(OH)_2 \qquad (6.12)$$

$$5Mg(OH)_2 + 4CO_2(aq\ and/or\ g) \rightleftharpoons Mg_5(CO_3)_4(OH)_2 \cdot 4H_2O. \qquad (6.13)$$

In these equations, "aq or g" indicates that the H_2O or CO_2 that reacts with MgO and/or brucite could be present in the aqueous phase (brine) and/or the gaseous phase. The brucite-hydromagnesite carbonation reaction (6.13) will buffer (control) the fugacity (essentially the partial pressure) of CO_2 at a relatively low value of about $10^{-5.50}$ atm if significant microbial activity occurs. If microbial activity occurs, the predicted value of f_{CO_2} will be identical for both Salado and Castile brine. The brucite-hydromagnesite buffer will control f_{CO_2} effectively because: (1) the DOE is emplacing more than enough MgO to ensure the consumption of essentially all CO_2 that could be produced in the repository, and (2) the reactivity of the MgO being emplaced in the WIPP is such that its carbonation rate exceeds the CO_2 production rate. The brucite dissolution reaction

$$Mg(OH)_2 \rightleftharpoons Mg^{2+} + 2OH^- \qquad (6.14)$$

will buffer the pH at about 9 in both Salado and Castile brine if microbial activity occurs (see Appendix PA, Attachment SOTERM, Section 2). For the CRA-2004 PA vectors with microbial activity, the composition of Salado or Castile brine at equilibrium with major Salado minerals such as halite and anhydrite, the f_{CO_2} established by Reaction 13, and the pH established by Reaction 6.14, have been used to calculate actinide solubilities.

In the absence of microbial activity, the carbonation reaction

$$Mg(OH)_2 + Ca^{2+} + CO_2(aq\ and/or\ g) \rightleftharpoons CaCO_3 + Mg^{2+} + H_2O(aq\ or\ g) \qquad (6.15)$$

will buffer f_{CO_2} at $10^{-5.48}$ atm in Salado brine and at $10^{-6.15}$ atm in Castile brine. Reaction 6.14 will buffer the pH at about 9 in both Salado and Castile brine (see Appendix PA, Attachment SOTERM, Section 2). For the 2004 PA vectors without microbial activity, the composition of Salado or Castile brine at equilibrium with major Salado minerals, the f_{CO_2} established by Reaction 6.15, and the pH established by Reaction 6.14, have been used to calculate actinide solubilities.

There is a relatively small amount of portlandite $Ca(OH)_2$ associated with the Portland cement used to dewater process sludges. The quantity of portlandite is too small, however, to overcome the buffer capacity of the reactions described above.

An analysis was carried out to determine the MgO safety, defined by:

$$MgO\ safety\ factor = (MgO_{emplaced}) \div (MgO_{required}), \qquad (6.16)$$

where $MgO_{emplaced}$ is the quantity of MgO to be emplaced in the repository and $MgO_{required}$ is the quantity of MgO required to consume the maximum amount of CO_2 produced by microbial consumption of all of the emplaced cellulosic, plastic, and rubber materials. This analysis used: (1) current estimates of the total quantities of cellulosic, plastic, rubber materials,

nitrate (NO_3^-), and sulfate (SO_4^{2-}) in the TRU waste and waste containers present after closure of the repository; and (2) recent results from a laboratory study of the efficacy of MgO. This analysis yielded a MgO safety factor of 2.45 (Appendix BARRIERS, Section BARRIERS-2.0). Therefore, there will be more than enough MgO to ensure that the conditions described above will be established in the repository factor (see Appendix BARRIERS, Section BARRIERS-2.0).

The waste contains ~~chemical compounds, known as~~ organic ligands~~,~~ that ~~can~~ ***could*** ~~enhance the concentration of actinide ions by~~ form~~ing soluble~~ ***dissolved*** complexes ~~of~~ ***with*** ~~these ions~~ ***actinides and thus increase their solubilities***. ~~The ligands of concern in the repository are acetate, citrate, oxalate, and ethylenediaminetetraacetate (EDTA) because they are soluble in brine and are known to be present in the waste (see WCASection 8.11).~~ ***There are four organic ligands of potential concern in the waste: acetate, citrate, ethylenediaminetetraacetic acid (EDTA), and oxalate. These organic ligands could increase the solubilities of the actinides in the waste because: (1) they are soluble in aqueous solutions such as WIPP brines, and (2) they are known to form complexes with the actinides (see Appendix PA, Attachment SOTERM, Section SOTERM-5.0)*** ~~However, these organic ligands also bond strongly to other metal species known to be in the repository system. The DOE assumethat because of this competition effect, the organic ligands will have no significant impact on the repository performance (see Appendix SOTERM, Section SOTERM.5, and Appendix SCR, Section SCR.2.5.6, for discussion).~~ ***Therefore, the effects of acetate, citrate, EDTA, and oxalate have been included in the Fracture-Matrix Transport (FMT) calculations of actinide solubilities for the CRA-2004 PA. These organic ligands will also form complexes with dissolved, cationic species of several metals present in the repository. These metals will thus compete with the actinides for the binding sites on these organic ligands. The effects of two of these metals, Mg^{2+} and Ca^{2+}, have been included in the solubility calculations for the CRA-2004 PA. Including complexation of actinides and of Mg^{2+} and Ca^{2+} by acetate, citrate, EDTA, and oxalate in the solubility calculations for the CRA-2004 PA has confirmed the conclusion in the CCA that organics will not increase the solubilities of the actinides significantly (see CCA Appendix SOTERM, Section SOTERM.5.0).***

6.4.3.5 Dissolved Actinide Source Term

~~Analysis reported in Appendix WCA (Section WCA.3) has demonstrated that the mobility in brine of the following actinides may be significant in the performance assessment of the WIPP: Th, U, Np, Pu, Cm, and Am. Although commonly referred to as actinides in the waste inventory, these substances are almost always present in the waste as solid actinide oxides or solid actinide salts, and if they dissolve in the WIPP brines, they will dissolve as complex ions. Additional discussion of actinide solubility modeling and the oxidation state distribution of the actinides is presented in Appendix SOTERM (Sections SOTERM.3 and SOTERM.4, respectively).~~

~~Actinides may be mobilized either by dissolution in brine as aqueous species, by bioaccumulation or sorption onto colloidal particles, or by condensation into colloidal forms as actinide intrinsic colloids that could be carried by brine (see Section 6.4.3.6 for a discussion of colloidal actinides). The dissolved actinide source term model calculates the dissolved concentration of each actinide in solution by applying the modeled solubility for the particular oxidation state, as determined by the oxidation state distribution for that actinide, at the~~

~~repository conditions presented in Section 6.4.3.4. Several oxidation states are not stable in the chemically reducing conditions described in Section 6.4.3.4. The unstable oxidation states are Np(VI), Pu(V), Pu(VI), and Am(V), as described in Appendix SOTERM (Section SOTERM.4).~~

~~Thorium will exist only in the IV oxidation state (see Appendix SOTERM, Section SOTERM.4.1). Am and Cm will exist in only the III oxidation state (see Appendix SOTERM, Sections SOTERM.4.4 and SOTERM.4.5). For the remaining actinides, Pu, U, and Np, it is uncertain whether repository conditions will favor the lower or higher of the remaining oxidation states (see Appendix SOTERM, Sections SOTERM.4.2, SOTERM.4.3, and SOTERM.4.6). The DOE has captured the range of possible behavior by assuming that in half the realizations, conditions within the repository are extremely reducing and the solubility of all three of these actinides will be adequately represented by the solubility of their lower oxidation states. In the other half of the realizations, the solubilities of these actinides are well represented by the solubilities of the higher of the possible oxidation states. The factors controlling the aqueous actinide concentration in a possible oxidation state are equilibrium with anhydrite, halite, MgO, and brine.~~

~~The solubility of the actinides as a function of equilibrium between anhydrite, halite, MgO, and brine is calculated outside of the performance assessment using FMT, a computer code for calculating actinide concentration limits based on thermodynamic parameters. The parameters for FMT are derived both from experimental investigations specifically designed to provide parameter values for this model and from the published literature. FMT and its application are described in Appendix SOTERM (Section SOTERM.3.5). Table 6-11 presents a summary of solubility parameter values for each actinide oxidation state consistent with the assumptions regarding chemical conditions stated in this section and Section 6.4.3.4. These values are documented in Table 6-11 and in Appendix PAR(Parameters 36 through 45 and Table PAR-39). Details of the generation of Table 6-11 are given in Appendix SOTERM (Section SOTERM.3).~~

The actinide source term used in the CRA-2004 PA calculations represents the aqueous concentrations of thorium (Th), uranium (U), Pu, and americium (Am) in the repository. The source term is the sum of the dissolved species (solubility) and the mobile suspended (colloidal) species of each of these actinides (see Section 6.4.3.6). The source term represents the mobile concentrations of Th, U, Pu, and Am that could be released from the repository in brine.

The actinide source term is limited to those radionuclides that could significantly affect the long-term performance of the WIPP. These radionuclides are all isotopes of Th, U, Pu, and Am. Their potential effects on the long-term performance of the repository can be ordered as Pu ≈ Am >> U > Th (Helton 1998). Other actinides, especially neptunium (Np), were included in the laboratory and modeling studies used to develop the actinide source term because it was not known which actinides could significantly affect the long-term performance of the repository.

Although commonly referred to as "actinide," these radioelements are almost always present in the waste as solid actinide oxides or solid actinide salts and, if they dissolve in WIPP brines, will form complex species (usually referred to as "complexes") with nonradioactive, inorganic, dissolved species such as carbonate ion (CO_3^{2-}), chloride ion (Cl^-) or hydroxide ion (OH^-), or

~~**Table 6-11. Summary of Dissolved Actinide Solubilities (moles per liter) in Castile and Salado Brines[a]**~~

~~Actinides~~	~~Brine~~	~~Maximum~~	~~Minimum~~	~~Median[b] or Constant~~
~~Am(III), Pu(III), Cm(III)~~	~~Salado~~	~~1.46×10^{-5}~~	~~5.82×10^{-9}~~	~~4.73×10^{-7}~~
~~Pu(IV), Th(IV), U(IV)~~	~~Salado~~	~~1.11×10^{-4}~~	~~4.40×10^{-8}~~	~~3.58×10^{-6}~~
~~Np(IV)~~	~~Salado~~	~~-~~	~~-~~	~~4.40×10^{-6}~~
~~Np(V)~~	~~Salado~~	~~-~~	~~-~~	~~2.30×10^{-6}~~
~~U(VI)~~	~~Salado~~	~~2.19×10^{-4}~~	~~8.70×10^{-8}~~	~~7.07×10^{-6}~~
~~Am(III), Pu(III), Cm(III)~~	~~Castile~~	~~1.64×10^{-6}~~	~~6.52×10^{-10}~~	~~5.30×10^{-8}~~
~~Pu(IV)~~	~~Castile~~	~~1.51×10^{-7}~~	~~6.00×10^{-11}~~	~~4.88×10^{-9}~~
~~Th(IV)~~	~~Castile~~	~~-~~	~~-~~	~~6.00×10^{-9}~~
~~U(IV)~~	~~Castile~~	~~-~~	~~-~~	~~6.00×10^{-9}~~
~~Np(IV)~~	~~Castile~~	~~-~~	~~-~~	~~6.00×10^{-9}~~
~~Np(V)~~	~~Castile~~	~~-~~	~~-~~	~~2.20×10^{-6}~~
~~U(VI)~~	~~Castile~~	~~2.21×10^{-4}~~	~~8.80×10^{-8}~~	~~7.15×10^{-6}~~

~~[a] Inorganic chemistry controlled by the $Mg(OH)_2$—$MgCO_3$ pair.~~
~~[b] Appendix SOTERM (Sections SOTERM.3.6 and SOTERM.7.2) discusses the relationship of this distribution to the modeled solubility.~~

with nonradioactive, organic, dissolved species such as acetate, citrate, EDTA, or oxalate (see Section 6.4.3.4).

The postclosure chemical environment in the repository will be strongly reducing (see Section 6.4.3.4; Appendix PA, Attachment SOTERM, Section SOTERM-2.0). Previous studies of actinide chemistry imply that, under these conditions, Th will exist as Th(IV) (Appendix PA, Attachment SOTERM, Section 4.1); U will exist as U(IV) or U(VI) (Section 4.2); Np will speciate as Np(IV) or Np(V) (Section 4.3); Pu will exist as Pu(III) and Pu(IV) (Section 4.4); and Am will speciate as Am(III) (Section 4.5). Several actinide oxidation states will be unstable under the strongly reducing conditions expected in the repository. These include Np(VI), Pu(V), Pu(VI), and Am(V). Pu(V) and Pu(VI) could occur in isolated microenvironments in the repository, however, the DOE concludes that would not persist in significant quantities because diffusive transport through any brine present and (especially in the event of human intrusion) advective transport of brine would expose any oxidized Pu to reducing materials like metallic Fe from waste containers and Fe-based materials in the waste, Fe(II)-bearing solids produced by anoxic corrosion of metallic Fe, dissolved Fe(II) species, and metallic Al in the waste (Appendix SOTERM, Sections SOTERM-2 and SOTERM-4; Marcinowski 2001). Microbial activity, if it occurs, would also help create reducing conditions.

The DOE incorporated the uncertainties regarding the oxidation states of U and Pu in PA by assigning a probability of 0.5 that they will exist in the U(IV) and Pu(III) oxidation states, and a probability of 0.5 that these elements will speciate in the U(VI) and the Pu(IV) oxidation

states (see also Appendix PA, Section SOTERM-5.2). The oxidation state for both elements is selected by a single variable in the LHS. Therefore, in approximately half of the PA realizations, the oxidation states of the transported actinides are Th(IV), U(IV), Pu(III), and Am(III); and, in the other half of the realizations, the oxidation states are Th(IV), U(VI), Pu(IV), and Am(III).

Laboratory studies with neodymium(III) (Nd(III)), Am(III), and Cm(III) were used to develop a solubility model for the +III actinides, and this model was used to predict the solubilities of Pu(III) and Am(III). Similarly, Th(IV) was used to develop a solubility model for the +IV actinides, which was used for Th(IV), U(IV), Np(IV), and Pu(IV). Literature data for Np(V) were used to develop a solubility model for the +V actinides, which was used only for Np(V). The +V model was not used for other actinides because Pu(V) would not persist in significant quantities in the WIPP. Using the oxidation-state analogy to extend the +III and +IV solubility models to Pu(III) and to U(IV), Np(IV), and Pu(IV), respectively, is valid for these reasons: First, the chemical behavior, especially the speciation and solubilities, of Nd(III), Pu(III), Am(III), and Cm(III) is very similar. Second, the chemical behavior of Th(IV), U(IV), Np(IV), and Pu(IV) is similar, although the solubility of Th(IV) is higher those of U(IV), Np(IV), and especially Pu(IV). Third, Nd, Am, and Cm speciate only in the +III oxidation state, and Th speciates only in the +IV oxidation state under typical laboratory conditions, thus making experiments with these actinides much easier to carry out and interpret than those with actinides that occur in more than one oxidation state, such as Pu.

The FMT calculations of actinide solubilities for the CRA-2004 PA featured the establishment of equilibrium of Salado brine (GWB) or Castile brine (ERDA-6) with halite and anhydrite, minerals present in large quantities in the Salado at the repository horizon. (These brines are described in Appendix PA, Attachment SOTERM, Section SOTERM-2.2.1). The effects of the MgO included the equilibrium of Salado brine or Castile brine with brucite and hydromagnesite ($Mg_5(CO_3)_4(OH)_2{\cdot}4H_2O$) in the performance-assessment vectors with microbial activity, and with brucite and calcite in the vectors without microbial activity (see Appendix BARRIERS, Section 2; and Appendix PA, Attachment SOTERM). For the 1997 PAVT, it was assumed that Salado brine (Brine A) or Castile brine (ERDA-6) would be in equilibrium with brucite and hydromagnesite ($Mg_5(CO_3)_4(OH)_2{\cdot}4H_2O$) in all of the performance-assessment vectors (both with and without microbial activity) (EPA 1998a, 1998b). For the CCA, equilibria among Salado brine (Brine A) and Castile brine (ERDA-6) and brucite and magnesite were assumed (CCA Appendix BACK).

The FMT calculations for the CRA-2004 PA also included the effects of acetate, citrate, EDTA, and oxalate on the speciation and solubilities of the +III, +IV, and +V actinides (see Appendix PA, Attachment SOTERM). The FMT calculations for the CCA PA and the 1997 PAVT did not include organic ligands.

Table 6-13 provides the solubilities calculated for the +III, +IV, and +V actinides and estimated for the +VI oxidation state for the CRA-2004 PA, and compares them to the solubilities calculated or estimated for the CCA PA and the 1997 PAVT. An uncertainty range of +1.4 orders of magnitude and -2.0 orders of magnitude was applied to the FMT predictions for the CRA-2004 PA (see Appendix PA, Attachment SOTERM, Section SOTERM-3.6). This

Table 6-13. Actinide Solubilities (M) Calculated (+III, +IV, and +V) or Estimated (+VI) for the CRA-2004 PA, the 1997 PAVT, and the CCA

Actinide Oxidation State and Brine	CRA-2004 Solubilities, Microbial Vectors[1]	CRA-2004 Solubilities, Nonmicrobial Vectors[1]	1997 PAVT Solubilities[2]	CCA Solubilities[3]
+III, Salado brine	3.07×10^{-7}	3.07×10^{-7}	1.2×10^{-7}	5.82×10^{-7}
+III, Castile brine	1.69×10^{-7}	1.77×10^{-7}	1.3×10^{-8}	1.3×10^{-8}
+IV, Salado brine	1.19×10^{-8}	1.24×10^{-8}	1.3×10^{-8}	4.4×10^{-6}
+IV, Castile brine	2.47×10^{-8}	5.84×10^{-9}	4.1×10^{-8}	6.0×10^{-9}
+V, Salado brine	1.02×10^{-6}	9.72×10^{-7}	2.4×10^{-7}	2.3×10^{-6}
+V, Castile brine	5.08×10^{-6}	2.13×10^{-5}	4.8×10^{-7}	2.2×10^{-6}
+VI, Salado brine[4]	8.7×10^{-6}	8.7×10^{-6}	8.7×10^{-6}	8.7×10^{-6}
+VI, Castile brine[4]	8.8×10^{-6}	8.8×10^{-6}	8.8×10^{-6}	8.8×10^{-6}

[1] *Brush and Xiong (2003a) and Downes (2003a,b).*

[2] *Trovato (1997, Attachment 2), U.S. EPA (1998a, Table 5), U.S. EPA (1998b, Subsection 4.10.4, Tables 4.10-1, 4.10-3 and 4.10-4; and Subsection 12.4, Table 12.4-1), and U.S. EPA (1998c, Subsections 5.26–5.32 and Section 6.0, Table 6.4).*

[3] *CCA Appendix SOTERM, Table SOTERM-2; based on Novak et al. (1996, Table 1, columns entitled "@Mg"), except that Novak et al. (1996) used molal instead of molar units.*

[4] *Hobart and Moore (1996).*

is the same uncertainty range used for the CCA PA and the 1997 PAVT. LHS was used to sample solubilities from these ranges.

A thermodynamic speciation and solubility model was not developed for U(VI); instead, literature data estimated the solubilities of U(VI) in the repository (Appendix PA, Attachment SOTERM, Section SOTERM-3.0; based on Hobart and Moore [1996]). These estimates have not been used for other actinides in the repository because Np and Pu will not persist in significant quantities in the +VI oxidation state.

~~Actinide concentration may not be equal to the values sampled in LHS. This condition could arise when there are not sufficient actinides in the solid phase~~ in a particular cell, when ~~combined with the dissolved actinides that may have been transported into that cell from an adjacent cell, to achieve the concentration value~~ as ~~determined by LHS sampling. This situation is referred to as inventory limited.~~

The actinide inventory is depleted on a cell-by-cell basis by the computer code NUTS (NUclide Transport Systems) for the undisturbed, E1, and E2 scenarios. The treatment of the E1E2 scenario is described in Section 6.4.13.5. In a computational cell, the processes affecting ~~actinide~~ dissolved ***actinide*** concentration***s*** are dissolution of solid actinide compounds, advection of dissolved actinides by brine flow from neighboring cells, and interaction with colloidal particles (see Section 6.4.3.6). NUTS dissolves each actinide until the maximum concentration determined by the actinide-source-term algorithms is obtained or an inventory limit is reached. In the repository, the transfer of actinides between solid phase***s*** and solution is tracked to preserve mass balance of the actinide inventory. Outside the repository, the model does not

precipitate actinides into the solid phase, thereby giving a conservative measure of mobile actinide ~~quantities~~ ***concentrations*** (see Appendix ***PA, Attachment*** SCR, ~~Section SCR.2.5.3.2~~ ***FEP W59***).

See Appendix PA, Attachment SOTERM, Section SOTERM-7.0, for a detailed description of the implementation of the actinide source term in PA.

6.4.3.6 Source Term for Colloidal Actinides

Colloidal actinides are discussed in greater detail in Appendix ***PA, Attachment*** SOTERM ~~(~~Section ~~SOTERM.~~6~~)~~. Colloidal particles form in the repository ~~by~~ ***through*** a variety of processes, including waste degradation, microbial activity, rock decomposition, and chemical condensation. These particles may also be carried into the repository by liquids moving from the Salado or through boreholes. Because of the presence of soils, nutrients, and cellulosic substrates for microbial action in WIPP waste (see Appendix ***TRU WASTE*** ~~BIR~~), humic substances and microbes will be present in disposal room brines, or may form in situ. Actinide-intrinsic colloids may form in the disposal rooms from condensation of dissolved actinides. Mineral fragments, as well as humic substances and microbes, may provide surfaces on which dissolved actinides ~~may~~ ***could*** sorb.

Four types of colloidal particles are believed to cover the range of possible behavior of all colloid types (see Appendix ***PA, Attachment*** SOTERM~~, Section SOTERM.6.1.2~~). The four particle types considered in ~~performance assessment~~***PA*** are microbes, humic and fulvic acids (humic substances), actinide-intrinsic (intrinsic), and mineral fragments. The concentration of actinides carried by each colloidal particle type depends on many of the same chemical conditions that govern the concentration of dissolved actinides.

Actinide concentrations associated with humic substances and microbes are linked to dissolved actinide concentrations through proportionality constants based on experimental results. For humic substances, actinide complexation constants from WIPP-specific experiments or ~~from~~ published literature are coupled with experimentally determined site-binding densities and solubilities of different types of humic substances in WIPP brines. For microbes, actinide uptake was experimentally determined through experiments with WIPP-relevant bacteria cultures. Actinide concentrations associated with mineral fragment-type colloidal particles are ~~estimated~~ based on results from experiments designed to determine mobile concentrations in brines, coupled with site-binding densities of mineral substrates. For the ~~Pu(IV) polymer~~ ***plutonium(IV) polymer***, actinide concentrations are determined through solubility experiments conducted from over- and ~~undersaturation over a range of~~ ***undersaturated ranges of*** pmH values. Intrinsic colloids of other actinides were determined to be ~~of~~ negligible ~~importance~~ and are eliminated from ~~performance assessment~~***PA*** calculations. For more discussion on this topic, refer to Appendix ***PA, Attachment*** SOTERM ~~(Section SOTERM.6.3.2.2~~).

Actinides associated with microbes and humics are related to the concentration of dissolved actinides in the repository through proportionality constants determined from interpretation of WIPP-relevant experiments and the literature (Appendix ***PA, Attachment*** SOTERM, ~~Sections SOTERM.6.3.3 and SOTERM.6.3.4~~). The proportionality-constant relationship is not based ~~rigorously~~ on thermodynamic equilibrium but is simply an empirical relationship. The

concentration of actinides associated with the ~~Pu(IV) polymer~~ ***plutonium(IV) polymer*** is a constant value determined from experimental results at the pmH conditions dictated by the presence of ***the*** MgO ~~backfill~~ ***engineered barrier***. Likewise, the concentration of actinides associated with mineral colloids is also a constant value, not linked to the concentration of dissolved actinides. Actinides associated with humics and microbes represent most of the colloidal actinide source term. Consequently, the colloidal actinide source term is closely related to the dissolved actinide source term. As discussed in Section 6.4.6.2, however, the source terms are considered separately for transport in the Culebra.

For ~~performance assessment~~***PA***, the concentration of each actinide element on each colloidal particle type during a realization is a fixed value. The concentration parameters are summarized in ~~Table 6-12~~***Table 6-14***. Actual values of actinide concentration***s*** on colloidal particles are constrained by inventory limits.

The concentrations of colloidal actinides indicated in this section are assumed to be ~~concentrations of~~ actinides mobilized on colloidal particles. The indicated concentrations will be entrained in moving brine. For conservatism, it is assumed that no actinides sorb onto colloidal particles that are not mobile in the repository. Thus, all actinides in the repository will be present in the solid phase, dissolved in the aqueous phase, or ~~as~~ colloidal actinides suspended in the aqueous phase.

When actinide inventory in a model cell is sufficient, the concentration of colloidal actinides will be at the values indicated in ~~Table 6-12~~***Table 6-14***. The total concentration of an actinide in solution and suspension is limited by the amount of solid***s*** available ~~to dissolve~~ from the inventory. This condition is called ***"***inventory-limited***."*** ~~when it occurs.~~

Colloid concentrations are calculated by the source-term procedure described in Appendix ***PA, Section SOTERM-4.3.2.*** ~~SOTERM (Sections SOTERM.7.1.4 and SOTERM.7.2).~~ Processes affecting the transport of colloids in the Culebra are addressed in Section 6.4.6.2.2.

6.4.4 Shafts and Shaft Seals

The four shafts connecting the repository to the surface are represented in ~~performance assessment~~***PA*** with a single shaft, represented by ***two primary regions above the repository,*** ~~Regions 2 through 11~~ ***and a concrete monolith*** ~~on (~~Figures 6-14 and 6-15***)***. This single shaft has a cross section and volume equal to the total cross section and volume of the four real shafts it represents and is separated from the waste disposal regions ~~in the model~~ by the true north-south distance from the waste to the nearest shaft (the Waste Shaft). Upon closure of the repository, the shafts will be sealed as described in Section 3.3.1. The seal system ***was originally*** ~~is~~ represented in ***the CCA PA*** by ~~discretizing~~ 11 ***discrete*** model***ed*** regions in the shaft. ***The representation was simplified by modeling the behavior of these 11 regions with two primary regions (Upper Shaft and Lower Shaft in Figures 6-14 and 6-15) that have properties simulating the behavior of the original 11 regions (see Appendix PA, Section PA-4.2.7). An analysis of the CCA results concluded that no significant flow of gas or brine would occur within the shaft seal system over the 10,000-year regulatory period. The new shaft model underwent peer review as required by 40 CFR § 194.27 and was incorporated in BRAGFLO (see Appendix PA, Section PA-4.2.7; Section 9.3.1.3.4; and Appendix PEER). The current***

Table *6-14*~~6-12~~. Colloid Concentration Factors

	Concentration on Mineral Fragments[a] *1*	Concentration as Intrinsic Colloid[a] *1*	Proportion Sorbed on Microbes[b] ~~2~~ [e] *5*	Maximum Sorbed on Microbes[c] *3*	Proportion Sorbed on Humics[b] *2*		Maximum Sorbed on Humics[a] *1*
					Salado	Castile	
Th(IV)	2.6×10^{-8}	0.0	3.1	0.0019	6.3	6.3	1.1×10^{-5}
U(IV)	2.6×10^{-8}	0.0	0.0021	0.0021	6.3	6.3	1.1×10^{-5}
U(VI)	2.6×10^{-8}	0.0	0.0021	0.0023	0.12	0.51	1.1×10^{-5}
Np(IV)	2.6×10^{-8}	0.0	12.0	0.0027	6.3	6.3	1.1×10^{-5}
Np(V)	2.6×10^{-8}	0.0	12.0	0.0027	9.1×10^{-4}	7.4×10^{-3}	1.1×10^{-5}
Pu(III)	2.6×10^{-8}	0.0	0.3	6.8×10^{-5}	0.19	1.37d	1.1×10^{-5}
Pu(IV)	2.6×10^{-8}	1.0×10^{-9}	0.3	6.8×10^{-5}	6.3	6.3	1.1×10^{-5}
Am(III)	2.6×10^{-8}	0.0	3.6	NA	0.19	1.37d	1.1×10^{-5}

[a] *1* In units of moles colloidal actinide per liter

[b] *2* In units of moles colloidal actinide per mole dissolved actinide

[c] *3* In units of moles total mobile actinide per liter

[d] *4* A cumulative distribution from 0.065 to 1.60 with a mean value of 1.1 was used.

[e] *5* ***Microbial colloids are not included in futures*** ~~that do not have~~ ***without microbial gas generation.***

NOTE: The colloidal source term is added to the dissolved source term to arrive at a total source term. Mineral fragments were provided with distributions, but the maximum was used as described in Appendix ***PA, Attachment*** SOTERM ~~(Section SOTERM.7.1.3)~~. Humic proportionality constants for III, IV, and V were provided with distributions, but only the Castile Am(III) and Pu(III) were sampled.

model divides the shaft into an upper region with all elements above the Salado and a lower region with all Salado elements. These regions are assigned material property distributions that represent the combined properties of all the individual materials in series. ~~These regions are as follows: an earthen fill region above the Rustler; a compacted clay column in the Rustler; an asphalt region at the top of the Salado; three concrete sections within the Salado; an upper Salado compacted clay column; a thick section of compacted crushed salt; a lower Salado compacted clay column separated into upper and lower segments; and a concrete monolith at the repository horizon (see Appendix SEAL, Section 4 and Appendix A). The concrete components in the Salado represent the concrete asphalt waterstops in the seal system design.~~ Seal material parameter values used in the PA are provided in ***Table 6-15*** ~~Table 6-13~~**.**

Conceptually, the shafts are assumed to be surrounded by a DRZ in the Salado. Within the bedded halite, the DRZ begins to form immediately after excavation and develops progressively ~~as a function of~~ ***from*** unloading as the formation creeps toward the excavated area. From a sealing perspective, the most important characteristic of the DRZ is the higher permeability that results from dilatant deformation and ~~the~~ increased pore volume.

The properties of the DRZ are known to vary with the type of adjacent material, time, and depth. When the shaft seals are emplaced, back pressures will progressively develop ~~over time~~ as the surrounding salt creeps inward. The back pressure applied by the seal material will progressively reduce the magnitude of the stress differential, which is the source for the DRZ microfracturing mechanism. The back pressure also results in a higher mean stress, which induces ~~of the~~ DRZ healing. The shaft DRZ permeability will, over time, approach that of the

intact halite. Also, since the creep rate of the salt surrounding the shafts depends on depth, the back pressures supplied by the seal materials will result in DRZ healing at rates that increase with depth. The relative stiffness of the seal material is a factor, as well.

~~In the performance assessment model, the radial extent of the DRZ around the shaft seal materials is an input parameter obtained by numerical model calculations and is corroboratedby field data (see Appendix SEAL, Section 8 and SEAL Appendix C). The permeability of the DRZ around the shaft versus distance is assumed to follow a log linear relationship. Permeability of the DRZ at the shaft wall is based on experimental data collected in the air intake shaft (Dale and Hurtado 1996) and Room M (Van Pelt 1995). More information on how the DRZ is incorporated into the shaft parameters is contained in Appendix PAR (Parameter 12).~~

The DRZ surrounding the shaft is not ***explicitly*** represented ~~explicitly~~ in the BRAGFLO mesh (Figures ~~6-13 to 6-15~~***6-14 and 6-15***). Rather, the mesh ~~has been~~ ***was*** simplified to represent only the cross-sectional area of the four WIPP shafts, and the permeability values ~~for~~ ***of*** the ~~various~~ seal components at different times have been adjusted ***(in the parameter database)*** to account for the ~~presence of the~~ shaft DRZ. This adjustment, which yields effective permeabilities, can be done because in Darcy flow, the flux through a porous medium is a linear function of the product ~~of the permeability of the medium~~ ***of the permeability*** and the cross-sectional area across which flow occurs. Thus, the flux that would occur through a shaft and its surrounding DRZ can be modeled equivalently using the shaft cross-sectional area with a higher seal component permeability. Equations for the derivation of the effective permeabilities are given in ***Appendix PA,*** ~~Appendix~~ ***Attachment*** PAR (Parameter***s 64 and 65).*** ~~12) and Appendix IRES (Section IRES.2). The permeabilities of shaft components are calculated in the SCMS (see Section 6.4.11) from LHS parameter values according to these equations. Appendix IRES (Section IRES.2) shows calculated shaft component effective permeabilities.~~

6.4.5 The Salado

The Salado is the principal natural barrier to fluid flow between the waste disposal panels and the accessible environment. Fluid flow in ***the Salado under*** natural ***(undisturbed)*** conditions ~~in the Salado~~ is discussed in Section 2.2.1.3. ~~Excavation of the r~~***R***epository ***excavation*** has altered natural pressure gradients in the Salado, creating the potential for fluid flow into the excavation. Fluid flow, gas generation, and volume changes from creep closure ~~cause changes~~ ***alter the*** ~~in~~ pressure gradients through time. Salt creep, as well as possible fracturing from high repository pressure, alters the permeability and other flow properties of the rock near the repository. Depending on pressure gradients ~~developed~~ and altered material properties, gas and brine flow may be enhanced in affected portions of the Salado.

For ~~performance assessment~~***PA***, the DOE conceptualizes the Salado as a porous medium composed of several rock types arranged in layers, through which flow occurs according to Darcy's law. Two rock types, impure halite and anhydrite, are used to represent the intact Salado. Once sampled, model parameters for all layers are uniform and constant, with two exceptions: porosity and permeability. ~~Conceptually, this~~ ***The*** assumption of constant properties is based on ~~observations of~~ ***observed*** compositional and structural regularity in layers exposed by the repository and on ~~the inference that there is~~ ***inferred small*** ~~little~~ variation ~~in large-scale averages of rock or flow properties across the disposal system~~. For several meters above and

Table *6-15*~~6-13~~. Shaft Materials Parameter Values

Parameter (units)	Maximum	Minimum	Median or Constant
UPPER ~~**ALL**~~ **SHAFT MATERIAL**~~**S**~~			
Residual Brine Saturation, S_{br} (unitless)	0.6	0	0.2
Residual Gas Saturation, S_{gr} (unitless)	0.4	0	0.2
Maximum Capillary Pressure (pascals)~~[a]~~ *[1]*	–	–	10^8
Permeability (square meters) ~~Pore Distribution, λ (unitless)~~	3.16×10^{-17} ~~8.10~~	3.16×10^{-21} ~~0.11~~	5.01×10^{-19} ~~0.94~~
Porosity (percent) ~~Threshold Pressure, Pt (pascals)~~	–	–	***29.1*** ~~0~~
LOWER ~~**CLAY**~~ **SHAFT MATERIAL**~~**S**~~ ***(0 to 200 years)***			
Initial Brine Saturation, (unitless) ~~Permeability (square meters) – Rustler Compacted Clay[b]~~	~~5×10^{-18}~~	~~1.0×10^{-21}~~	5.34×10^{-1} ~~5×10^{-19}~~
Permeability (square meters)~~[b]~~ *[2]* ~~– Upper Salado Compacted Clay[b]~~	3.16×10^{-17} ~~5×10^{-18}~~	1.0×10^{-20} ~~1.0×10^{-21}~~	6.31×10^{-19} ~~5×10^{-19}~~
~~Permeability (square meters) – Lower Salado Compacted Clayb~~	~~5 × 10−18~~	~~1.0 × 10−21~~	~~5 × 10−19~~
Maximum Capillary Pressure (pascals)[1]	–	–	10^8
~~Permeability (square meters) – Bottom Clay[b]~~	~~5 × 10−18~~	~~1.0 × 10−21~~	~~5 × 10−19~~
~~Thickness (meters) – Rustler Compacted Clay~~	–	–	~~94.3~~
~~Thickness (meters) – Upper Salado Compacted Clay~~	–	–	~~104.85~~
~~Thickness (meters) – Lower Salado Compacted Clay~~	–	–	~~23.9~~
~~Thickness (meters) – Bottom Clay~~	–	–	~~9.24~~
Effective Porosity (percent) ~~– All Clays~~	–	–	***11.3*** ~~24.0~~
~~Pore Volume Compressibility (1/pascals) – Rustler Compacted Clay~~	–	–	~~1.96 × 10−9~~
~~Pore Volume Compressibility (1/pascals) – Upper Salado Compacted Clay~~	–	–	~~1.81 × 10−9~~
~~Pore Volume Compressibility (1/pascals) – Lower Salado Compacted Clay and Bottom Clay~~	–	–	~~1.59 × 10−9~~
LOWER ~~**SALT**~~ **SHAFT MATERIAL** ***(200 to 10,000 years)***			
Initial Brine Saturation, (unitless) ~~Permeability (square meters) – Salt[b]~~	~~2×10^{-18}~~	~~1×10^{-23}~~	5.34×10^{-1} ~~5.4×10^{-21}~~
Permeability (square meters)[2]	1×10^{-18}	3.16×10^{-23}	7.94×10^{-21}
Maximum Capillary Pressure (pascals)[a] ~~Thickness (meters) – Salt~~	–	–	10^8 ~~171.37~~
Effective Porosity (percent) ~~– Salt~~	–	–	***11.3*** ~~5.0~~
~~Pore Volume Compressibility (1/pascals) – Salt~~	–	–	~~1.60 × 10−9~~
~~**CONCRETE SHAFT MATERIALS**~~			
~~Permeability (square meters) – Concrete (T < 400 years)~~	~~1 × 10−17~~	~~1 × 10−23~~	~~1.78 × 10−19~~
~~Permeability (square meters) – Concrete (T > 400 years) and Concrete Monolith~~	–	–	~~1 × 10−14~~

Table *6-15*~~6-13~~. Shaft Materials Parameter Values — Continued

Parameter (units)	Maximum	Minimum	Median or Constant
~~Thickness (meters) – Concrete~~	–	–	~~45.72~~
~~Thickness (meters) – Concrete Monolith~~	–	–	~~9.08~~
~~Effective Porosity (percent)~~	–	–	~~5.00~~
~~Threshold Pressure Pt (pascals) – All Concretea~~	–	–	~~0~~
~~Pore Volume Compressibility (1/pascals) – All Concrete~~	–	–	~~2.64 × 10−9~~
~~**ASPHALT SHAFT MATERIAL**~~			
~~Permeability (square meters) – (T = 0 – 10,000 years)~~	~~10−18~~	~~10−21~~	~~10−20~~
~~Thickness (meters)~~	–	–	~~37.28~~
~~Effective Porosity (percent)~~	–	–	~~1.00~~
~~Pore Volume Compressibility (1/pascals)~~	–	–	~~2.97 × 10−8~~
~~**EARTHEN FILL MATERIAL ABOVE RUSTLER**~~			
~~Permeability (square meters) (T = 0 – 10,000 years)~~	–	–	~~1 × 10−14~~
~~Thickness (meters)~~	–	–	~~165.06~~
~~Effective Porosity (percent)~~	–	–	~~32.0~~
~~Pore Volume Compressibility (1/pascals)~~	–	–	~~3.1 × 10−8~~

~~a~~[1] Capillary pressure for all shaft materials is set to 0.

~~b~~[2] These values represent the permeabilities of the seal material ~~without~~ ***incorporating*** the surrounding DRZ ~~incorporated. See Appendix IRES, Section IRES.2, for time-dependent values.~~

below the repository, a DRZ has ~~increased~~ ***higher*** permeability ~~compared to~~ ***than*** intact rock and offers little resistance to flow between anhydrite interbeds and the repository. ~~In all rock units,~~ ~~p~~***P***orosity can vary from ***its*** initial value~~s~~ due to ***pressure-dependent*** compressibility~~, depending on pressure changes in a computational grid block~~. As discussed in Section 6.4.5.2, a model has been implemented in interbeds to simulate the effects of fracturing caused by high repository pressure as pore pressure approaches or exceeds lithostatic.

Specific information about the three submodels used to represent impure halite, Salado interbeds, and the DRZ is presented in the following sections.

6.4.5.1 Impure Halite

The ~~DOE~~***PA*** uses a single porous medium with spatially constant rock and hydrologic properties (***labeled "Salado"*** ~~Region 19~~ in Figures ~~6-13 and 6-14~~***6-14 and 6-15***) in ~~performance assessment~~***PA*** to represent intact, halite-rich layers in the Salado and minor interbeds contained within ~~those~~ layers that are not explicitly represented. A comparison ~~has been~~ ***was*** made between the simplified stratigraphy used in the ~~performance assessment~~***PA*** model and a model with a more detailed stratigraphy in the vicinity of the repository~~:~~. ~~t~~***T***his comparison supports use of ~~the~~ stratigraphic representation ~~used~~ for ~~performance assessment~~***PA***. This model comparison is described in Christian-Frear and Webb (1996).

Gas may not be able to flow through intact, halite-rich strata of the Salado under realistic conditions for the repository. Gas flow in liquid-saturated rock depends on the gas pressure

required to overcome capillary resistance to initial gas penetration and ~~development of~~ interconnected gas pathways that allow gas flow (threshold pressure). While the permeability of halite is known to be low, its threshold pressure has never been measured. An empirical relationship between threshold pressure and permeability in non-WIPP rocks (Davies 1991, 17-19) suggests that threshold pressure will be ~~sufficiently~~ high ***enough*** that gas will ~~not~~ be ***un***able to flow through the halite-rich strata of the Salado under any conditions foreseeable for the WIPP ***(***see Appendix ***PA, Attachment*** MASS, Section MASS-13.1***)***. ***The DOE*** ~~V~~***v***alues ~~used by the DOE~~ for halite threshold pressure are consistent for generic material of low permeability and prevent ~~the flow of~~ gas ***flow*** into the impure halite regions (***Table 6-16***~~Table 6-14~~). This is a conservative assumption because gas flow in halite would decrease the pressure in the repository and the driving force available for flow elsewhere. ***Table 6-16***~~Table 6-14~~ shows various parameter values used in modeling the Salado impure halite. Additional information on parameter values is contained in Appendix ***PA, Attachment*** PAR (Parameters 17 through 19 and Table ***PAR-2*** ~~PAR-32~~).

Table *6-16*~~6-14~~. Salado Impure Halite Parameter Values

Parameter (units)[a 1]	Maximum	Minimum	Median or Constant
Permeability (square meters)	10^{-21}	10^{-24}	3.16×10^{-23}
Effective Porosity (percent)	3.0	0.10	1.0
Threshold Pressure, P_t (pascals)[~~b~~ 2]	1.13×10^{8}	1.03×10^{7}	3.41×10^{7}
Residual Brine Saturation, S_{br} (unitless)	***0.60***	***0***	0.3
Residual Gas Saturation, S_{gr} (unitless)	***0.40***	***0***	0.2
Pore Distribution Parameter, λ (unitless)	***1.0***	***0.20***	0.7
Maximum Capillary Pressure (pascals)	–	–	10^{8}
Rock Compressibility (1/pascals)[e 3]	1.92×10^{-10}	2.94×10^{-12}	9.75×10^{-11}

[a 1] See ***Table 6-11***~~Table 6-9~~ for fluid properties.

[~~b~~ 2] Threshold pressure (P_t) determined from the relationship: $P_t = PCT\_A \cdot k^{PCT\_EXP}$ where PCT_A and PCT_EXP are constants and k is the permeability.

[e 3] Pore compressibility = ***r***ock compressibility/effective porosity.

6.4.5.2 Salado Interbeds

Three distinct anhydrite interbeds are modeled in BRAGFLO, representing MB138 ***(see*** ~~(Region 20 in~~ Figures ~~6-13 and 6-14~~***6-14 and 6-15***), anhydrite layers a and b ***(Anhydrite AB)***~~(Region 21)~~, and MB139 ~~(Region 28)~~. The three ~~intact~~ interbeds have the same set of model parameters, and the parameters are initially spatially constant. Porosity and permeability can vary spatially during a simulation, depending on the extent of interbed fracturing. The interbeds differ only in position and thickness.

The three interbeds explicitly represented in the BRAGFLO model are included because they exist in the disturbed region, as modeled around the repository within which fluid is expected to be able to flow with relative ease compared to the surrounding formation. MB139 and anhydrite layers a and b are present within the DRZ that forms around excavations***, as shown by Park and Holland (2003) in their analysis of the effects of raising the repository horizon 2.34 meters***

(7.67 feet). MB138 is included along with a thick DRZ because of uncertainty in the extent and properties of the DRZ and the associated long-term isolation of MB138 from the repository. ***A more detailed examination of the DRZ was necessary to incorporate the Option D panel closure into the PA grid. Even though the DRZ would not reach MB 138, PA models the potential for a hydraulic connection between MB 138 and the repository through the DRZ.***

In BRAGFLO, brine flows between the Salado and the repository in response to fluid potential gradients that may form over time. Because of the ~~low permeability of the~~ impure halite***'s low permeability*** and relatively small surface area ~~involved~~, direct brine flow between the impure halite and the repository is relatively small. The interbeds included in the BRAGFLO model of the Salado, ~~(Regions 20, 21, and 28)~~ however, ~~can~~ serve as conduits for brine flow between the impure halite and the repository. Conceptually, brine flows laterally along higher permeability interbeds towards or away from the repository and vertically between the interbeds and the lower permeability halite. Because the interbeds have a very large contact area with adjacent halite-rich rock, even a very small flux from the halite into the interbeds (for brine inflow) or to the halite from the interbeds (for brine outflow) can accumulate ~~into a~~ significant ~~quantity~~ ***quantities*** of brine. In this manner, halite serves as a source or sink for brine in the repository. It is expected that, because of density differences between gas and brine and their stratification within the repository, brine outflow will be ***pre***dominantly in MB139, and gas outflow will occur in anhydrite a and b or MB138. However, the model does not preclude other flow patterns.

Interbeds contain natural fractures that may be partially healed~~.~~***, but anhydrite lithologies proximal to disposal rooms will be highly distorted as the rooms creep closed. Fractured and distorted anhydrite would not be expected to heal in a manner expected of the DRZ in salt.*** If high pressure is developed in an interbed, its preexisting fractures may dilate or new fractures may form, altering its porosity and permeability. Pressure-dependent changes in permeability are supported by experiments conducted in the WIPP ~~underground~~ and in the laboratory (Beauheim et al. 1993). Accordingly, the DOE has implemented in BRAGFLO a porous-media model of interbed dilation and fracturing that causes the porosity and permeability of a***n interbed's*** computational cell ~~in an interbed~~ to increase as its pore pressure rises above a threshold value. Model details are presented in Appendix ***PA, Section PA-4.2 and Attachment MASS, Section MASS-13.0.*** ~~BRAGFLO (Section 4.10) and Appendix MASS (Section MASS.13.3)).~~ To the extent that it occurs, ***interbed*** dilation or fracturing ~~of interbeds~~ is expected to increase the transmissivity of interbed intervals. The threshold pressure of dilated or fractured interbeds is expected to be low because apertures of the fractures increase; thus, fluid is expected to ~~be able to~~ flow outward readily if adequate pressure ~~is available to~~ dilate***s*** the interbeds.

The model used to simulate the effects of interbed dilation or fracturing is explained in detail in Appendix ~~BRAGFLO (Section 4.10)~~ ***PA, Attachment MASS, Section MASS-13.0***. In summary, it assigns a fracture initiation pressure above the initial pressure at which local fracturing takes place~~., and c~~***C***hanges in permeability and porosity occur above this pressure. Below this fracture initiation pressure, an interbed has the permeability and compressibility assigned by LHS ~~and representative of~~ ***to represent*** intact rock. Below the fracture initiation pressure, the initial sampled porosity is modified slightly with pressure caused by compressibility. Above the fracture initiation pressure, the local compressibility of the interbed is assumed to increase linearly with pressure. This greatly increases the rate at which porosity increases with increasing

pore pressure. Additionally, permeability increases by a power function of the ratio of altered porosity to initial porosity. For numerical reasons (that is, to prevent unbounded changes in parameter values that would create numerical instabilities in codes), a pressure is specified above which porosity and permeability change no further.

Parameters associated with the interbeds are shown in ***Table 6-17*** ~~Table 6-15~~**.** ***Table 6-18*** ~~Table 6-16~~ lists parameters used ~~in the~~ ***to*** model ~~of~~ interbed dilation and fracture. Additional information about interbed parameters is included in ***Appendix PA,*** ~~Appendix~~ ***Attachment*** PAR**,** ~~(~~Table ***2,*** ~~PAR-36~~ and Parameters 20 through 25~~)~~.

Table *6-17*~~6-15~~. Parameter Values for Salado Anhydrite Interbeds a and b, and MB138 and MB139

Parameter (units)[a] [1]	Maximum	Minimum	Median or Constant
Permeability (square meters)	7.94×10^{-18}	10^{-21}	1.29×10^{-19}
Effective Porosity (percent)	***1.7*** –	***0.60*** –	1.1
Threshold Pressure, P_t (pascals)[b] [2]	5.28×10^{6}	2.32×10^{5}	9.74×10^{5}
Residual Brine Saturation, S_{br} (unitless)	0.174	0.007~~846~~	0.084
Residual Gas Saturation, S_{gr} (unitless)	0.197	0.014	0.077
Pore Distribution Parameter, λ (unitless)	0.842	0.491	0.644
Maximum Capillary Pressure (pascals)	–	–	10^{8}
Rock Compressibility (1/pascals)[c] [3]	2.75×10^{-10}	1.09×10^{-11}	8.26×10^{-11}
~~Brine Far-Field Pore Pressure at elevation of MB139 and shaft intersection (pascals)~~	~~13.9 × 106~~	~~11.0 × 106~~	~~12.5 × 106~~

[a] [1] See ***Table 6-11*** ~~Table 6-9~~ for fluid properties.

[b] [2] Threshold pressure (P_t) determined from the relationship: $P_t = PCT\_A \cdot k^{PCT\_EXP}$ where PCT_A and PCT_EXP are constants and k is the permeability.

[c] [3] Pore compressibility = Rock compressibility/effective porosity.

Table *6-18*~~6-16~~. Fracture Parameter Values for Salado Anhydrite Interbeds a and b, and MB138 and MB139

Parameter (units)	Constant
Fracture initiation pressure at MB139, base of shaft (pascals)	12.7×10^{6}
Increment to give full fracture porosity (percent), MB139 and MB138[a] [1]	3.9
Increment to give full fracture porosity (percent), Anhydrite a and b[a] [1]	23.9
Full fracture permeability (square meters)	10^{-9}
Increment above fracture initiation pressure to obtain full fracture pressure (pascals)[a] [1]	3.8×10^{6}

[a] [1] A fitting parameter to yield desired dilation over a variation in pressure.

6.4.5.3 DRZ

In the DRZ (***see*** ~~Region 22 in~~ Figures ~~6-13~~***6-14*** and ~~6-14~~***6-15***) near the repository, permeability and porosity are expected to generally increase in both halite and interbeds. These increases are

due to a variety of processes. Creep closure and stress-field alterations as the result of the excavation are the dominant causes, similar to the processes discussed for ~~the formation of~~ ***forming*** the DRZ around the shaft (see Section 6.4.4). The increases in permeability and porosity in interbeds are not ~~expected~~ ***likely*** to be completely reversible with creep closure of the disposal rooms. The increase in DRZ permeability increases the ability of fluid to flow from interbeds to the waste disposal region. The increase in DRZ porosity provides a volume in which some fluid could be retained so that it does not contact waste or slows actinide movement.

~~Performance assessment~~ ***In approximating*** ~~approximates~~ the effects of the DRZ***,*** ~~performance assessment~~***PA*** conservatively ***overestimates*** ~~with respect to~~ brine flow to***ward*** the repository (see Appendix ***PA, Attachment*** MASS, Section ~~MASS~~ ***13***~~.13.4~~). In the model, the permeability of this region is increased relative to intact Salado rock for the duration of a realization. The porosity of the modeled DRZ is increased by a fixed value of 0.0029 (0.29 percent) above the sampled ***porosity of the*** intact Salado impure halite. The modeled DRZ extends above and below the repository from the base of MB138 to MB139***, thereby retaining the geometry used in the CCA and 1997 PAVT***. The ~~performance assessment~~***PA*** treatment of the DRZ creates a ~~permanent high-permeability~~ region that ***may allow fluid*** ~~does not significantly impede~~ flow between the repository and affected interbeds. ***Table 6-19***~~Table 6-17~~ shows parameter values used in the ~~performance assessment~~***PA*** representation of the DRZ.

Table *6-19*~~6-17~~. DRZ Parameter Values

Parameter (units)[a] [1]	Maximum	Minimum	Median or Constant
Permeability (square meters)	***3.16×10^{-13}*** –	***3.98×10^{-20}*** –	***10^{-16}*** ~~10^{-15}~~
Effective porosity (percent)[b] [2]	***3.3*** –	***0.04***	1.29
Threshold pressure, P_t (pascals)	–	–	0
Residual brine saturation, S_{br} (unitless)	–	–	0
Residual gas saturation, S_{gr} (unitless)	–	–	0
Pore distribution parameter, λ (unitless)	–	–	0.7
Maximum capillary pressure (pascals)	–	–	10^8
Rock compressibility (1/pascals)[c] [3]	–	–	7.41×10^{-10}

[a] [1] See ***Table 6-11***~~Table 6-9~~ for fluid properties.

[b] [2] The DRZ effective porosity value for each realization is equivalent to the sampled value for the Salado halite plus 0.0029 (0.0029 is the difference between the medians for the DRZ and the halite).

[c] [3] Pore compressibility = rock compressibility/effective porosity.

The DOE originally used a constant permeability for the DRZ over the 10,000-year regulatory time frame. However, the EPA required the DOE to treat the DRZ permeability as uncertain during the PAVT (EPA 1998, TSD V-B-14). The range is sampled to determine a fixed value for each realization over the 10,000-year period. Additionally, in the 1997 PAVT, the anhydrite fracture model was applied to the DRZ to capture the effects of halite fracture under high repository pressures. As was done in the 1997 PAVT, the CRA-2004 PA treats the DRZ permeability as an uncertain parameter, and the anhydrite fracture model is also applied to the DRZ. The parameter values are shown in Table 6-19.